Chapter 4

Spatial Distribution of Fault Kinematics along the Himalayan Arc

" *We learn geology the morning after the earthquake.*"

by Ralph Waldo Emerson

The present chapter focuses on the estimation of fault kinematics of the megathrusts along the Himalayan arc using a two-dimensional splay-fault Bayesian inversion model. The chapter concludes by computing the earthquake potential from the derived slip deficit rates.

Contents

Parts of this chapter have been submitted/published/under preparation in the following refereed publications:

1. **Y. Sharma**, S. Pasari, O. Dikshit, and K.E. Ching, "GPS-based monitoring of crustal deformation in Garhwal-Kumaun Himalaya", *ISPRS- International Archives of the Photogrammetry, Remote Sensing and Spatial Information Sciences*, vol. XLII-5, pp. 451-454, 2018. (Scopus)
   (https://doi.org/10.5194/isprs-archives-XLII-5-451-2018)

2. **Y. Sharma**, S. Pasari, K.E. Ching, and O. Dikshit, “Interseismic slip rate and fault locking along the Northwest Himalaya”, *Tectonophysics*. (In revision)

3. **Y. Sharma**, S. Pasari, and K.E. Ching "Kinematics of crustal deformation along the central Himalaya", *Natural Hazards*. (Under review)

4. **Y. Sharma**, S. Pasari, and K.E. Ching "Present-day crustal deformation along the Kumaun Himalaya: Role of Garampani-Kathgodam fault". (Under preparation)

4.1 Introduction

The continental thrust systems are capable of producing some of the destructive earthquakes around the tectonic boundaries of the world. The fault splay along these boundaries not only characterizes strain accumulation but also influences other factors, such as the fault geometry, slip distribution, and the level of stress transfer at the segment boundary [e.g., 46, 74]. Along the world's largest continent−continent collision boundary, the Himalaya, slip rates of the megathrust system are observed to be discontinuous along-strike, revealing significant variations in the crustal deformation pattern. Such along-strike irregularity and deformation variability of a fault system play key roles in earthquake potential estimation and consequent seismic hazard evaluation in a defined area [310]. In light of this, a better knowledge of slip segmentation and the underneath fault geometry, with a robust geodetic network and an elastic model, is indispensable to re-construct the regional-scale deformation and its implication on future seismic hazard [20]. In this regard, the present chapter addresses computation of slip rate distribution and fault geometry of the Himalayan megathrust system using a two-dimensional Bayesian splay-fault inversion model.

The Himalaya has been recognized to be a vital gateway for the future hazardous earthquakes [321]. In the last ∼200 years, it has experienced many major earthquakes, namely the 1803 Garhwal earthquake (M_w=7.5), 1905 Kangra earthquake (M_w=7.8), 1934 Bihar-Nepal earthquake (M_w=8.1), 1950 Assam earthquake (M_w=8.4), 2005 Kashmir earthquake (M_w=7.6), and the 2015 Nepal earthquake (M_w=7.8) [7, 8, 30, 29, 103, 129, 301]. Numerical simulations [e.g., 48, 61] indicate that the same section of the MHT, which has hosted past large earthquakes, can still generate moderate earthquakes ($M_w \sim$ 7.0) and even great events ($M_w \geq 8.0$).

The horizontal GPS velocity field (discussed in Section 3.5) is inverted in a 2D Bayesian dislocation model to understand the fault geometry, segment linkage, slip rate distribution, and earthquake potential of the megathrust system in the study region comprising 15 arc-normal transects (Fig. 4.1 to Fig. 4.3). The pattern of slip distribution can highlight (i) the locked portions of the seismogenic faults along which future earthquakes might strike, or (ii) interseismic creeping that can inhibit earthquake rupture propagation [e.g., 17, 54, 176, 277].

4.2 Dataset and study area

As mentioned before, the majority of crustal strain accumulation along the Himalayan region is accommodated by the mainstream thrust system of the Himalayan arc [30]. From north to south, the fault system comprises the MCT, MBT, and the MFT [321]. The above thrust system along the Himalaya (i.e., MCT, MBT, and MFT) is assumed to emanate from the top and merge beneath the Himalaya into a décollement, known as the MHT (Fig. 1.4) [321]. Previous geodetic studies [2, 20, 88, 154, 220, 277, 316] have suggested that the deeper part of MHT is creeping, while the shallower part (i.e., MFT) is locked with a slip deficit rate of $\sim$14$-$18 mm/yr. This deficit rate accumulated over a century is sufficient to produce a great Himalayan earthquake in the near future [154, 219, 277].

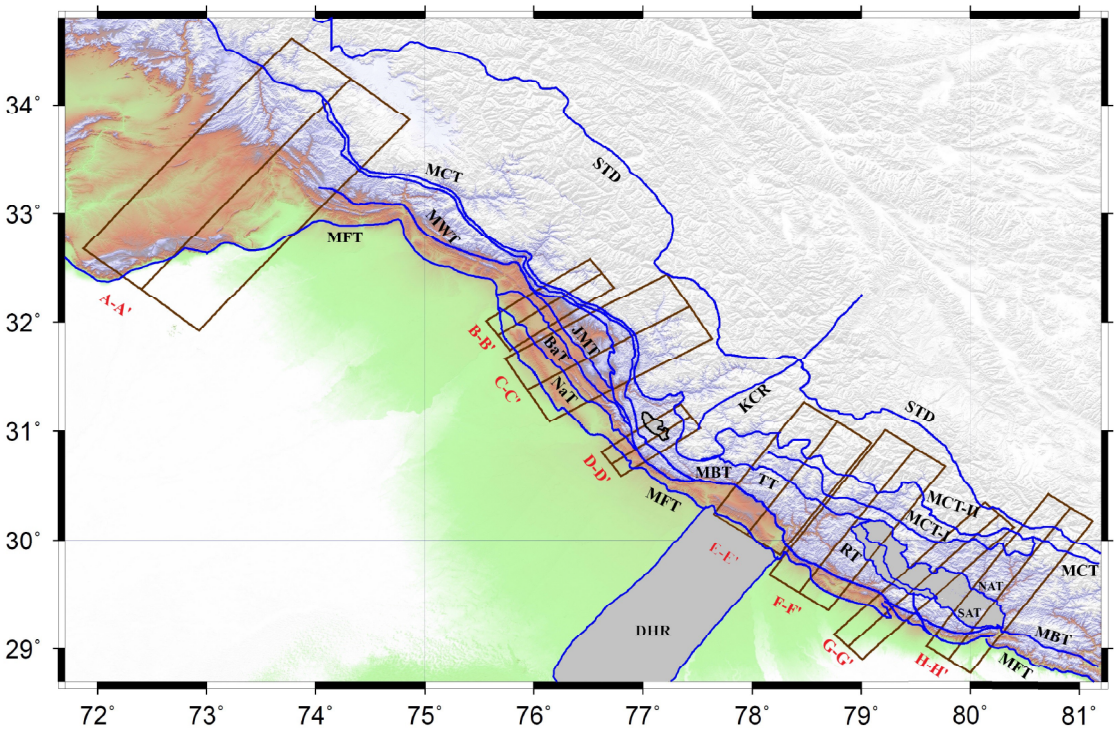

Fig. 4.1: Distribution of eight transects along the northwest Himalaya; brown rectangles represent the extent of transects. Abbreviations are as follows: BaT, Barsar Thrust; DHR, Delhi-Haridwar Ridge; JMT, Jawalamukhi Thrust; KCR, Kaurik Chango Rift; MBT, Main Boundary Thrust; MCT, Main Central Thrust; MFT, Main Frontal Thrust; MWT, Medilicott- Wadia Thrust; NaT, Nalagarh Thrust; NAT, North Almora Thrust; RT, Ramgarh Thrust; SAT, South Almora Thrust; STD, South Tibetan Detachment; TT, Tons Thrust.

To derive the spatial distribution of fault kinematics, the velocity field comprising 486 GPS stations has been used (see Section 3.5). With this velocity field, 15 arc-normal transects are used to estimate the geometrical configuration and slip distribution along the megathrust system (i.e., MFT, MBT, MCT, and MHT). There are eight transects (A-A', B-B', C-C', D-D', E-E', F-F', G-G', and H-H') along the northwest Himalaya (Fig. 4.1), five transects (I-I', J-J', K-K', L-L', and M-M') along the central Himalaya (Fig. 4.2), and two transects (N-N' and O-O') along the northeast Himalaya (Fig. 4.3). The configuration of each transect is summarized in Table 4.1.

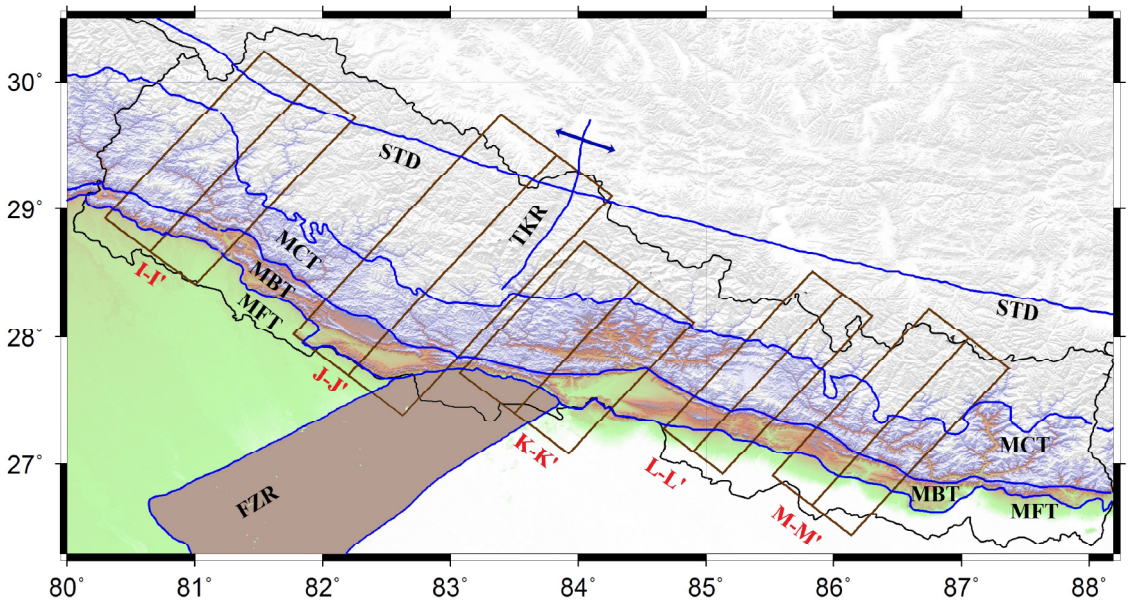

Fig. 4.2: Distribution of five transects along the central Himalaya; brown rectangles represent the extent of transects. Abbreviations are as follows: FZR, Faizabad Ridge; MSR, Munger-Saharsa Ridge; MBT, Main Boundary Thrust; MCT, Main Central Thrust; MFT, Main Frontal Thrust; STD, South Tibetan Detachment; TKR, Thakola Rift.

Table 4.1: The projection parameter (center coordinates, strike, azimuth, length, and width) and number of GPS velocity vectors in each profile

Transect	Number of Stations	Center coordinates		Strike (°)	Azimuth (°)	Length (km)	Width (km)
		Long (° E)	Lat (° N)				
A-A'	20	72.40	32.30	310	40	281	65

B-B’	7	75.67	31.88	325	55	110	18
C-C’	9	75.94	31.38	329	59	165	38
D-D’	8	76.71	30.70	325	55	85	15
E-E’	15	77.80	30.00	305	55	122	40
F-F’	10	78.43	29.52	305	35	180	32
G-G’	31	78.80	29.02	315	45	191	18
H-H’	16	79.80	28.90	305	35	190	24
I-I’	6	80.65	28.67	310	40	190	45
J-J’	14	82.20	27.70	310	40	250	55
K-K’	13	83.50	27.40	310	40	150	55
L-L’	12	84.90	27.10	310	40	180	30
M-M’	10	85.83	26.68	310	40	190	40
N-N’	12	88.20	26.70	310	40	235	25
O-O’	5	91.37	26.10	280	10	135	30

The details of these transects, the used methodology, results of 2D inversion modeling, and the estimated posterior probability distributions of the fault parameters are provided in the subsequent sections.

4.3 Methodology

Though the stress accumulation along the Himalayan arc may be governed by both elastic and inelastic processes [30], the present study characterizes fault parameters (i.e., slip rate, rake, dip angle, depth, location of fault at the surface, and locking depth) based on a purely elastic two-dimensional inversion model [199]. The horizontal velocities are inverted from 15 along-strike velocity profiles into fault slip rate and other fault geometries. These 15 transects are chosen keeping in mind the following points:

1. The Himalayan megathrust system should cross through these transects.

2. Each transect should cover sufficient number of GPS velocity vectors.

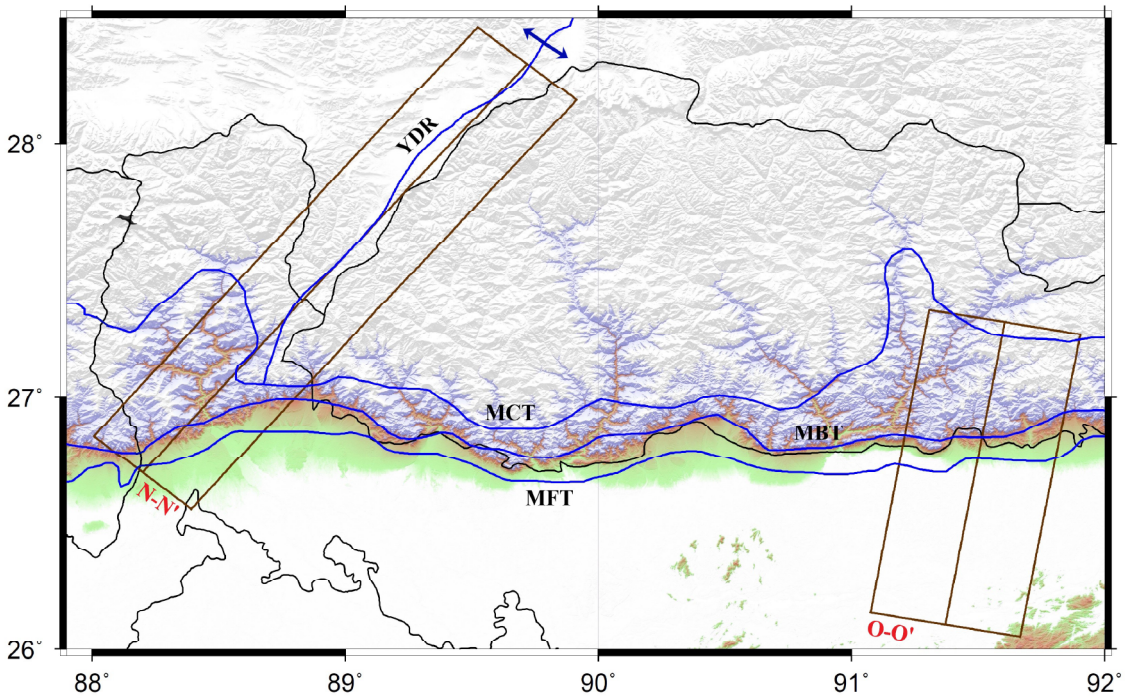

Fig. 4.3: Distribution of two transects along the northeast Himalaya; brown rectangles represent the extent of transects. Abbreviations are as follows: MBT, Main Boundary Thrust; MCT, Main Central Thrust; MFT, Main Frontal Thrust

In each profile, the relative surface velocity field is computed by fixing the southernmost station (e.g., in profile B-B', the MUKE station is fixed to calculate the relative velocity of other stations in this transect). The relative velocity for each profile is decomposed into two components: fault-normal and fault-parallel. The fault-normal component represents the arc-perpendicular surface velocity that accounts for the regional extension or compression, whereas the fault-parallel component indicates arc-parallel horizontal velocity that reveals information about strike-slip displacement [53].

For the inversion model, it is assumed that the non-planar fault geometry consists of a basal detachment along with several branching faults [53] (see Fig. 4.4). The sum of slip rates (S_{f1} and S_{f2}) of all the branching faults is assumed to be equal to the slip rate (S_d) of the detachment (Fig. 4.4). Due to the impact of fault fraction, the shallower portions of the branching faults are assumed to be locked, indicating strain energy accumulation in the interseismic period [53, 74]. The current model assumes that there is no slip rate for a segment that is shallower than the fault-locking depth. To estimate the fault slip rates using geodetic data below observation equation is utilized.

$$d = G(m) \times s + \varepsilon \tag{4.1}$$

Here, G is the matrix kernel (i.e., Green's function); m is a function of fault parameters (i.e., strike, dip, length, width, depth, rake, and fault surface location); d is the vector of observed surface displacements; s is the vector of fault slip (to be estimated); and ε represents normally (Gaussian) distributed errors with mean zero and covariance Σ_0 (i.e., $\varepsilon \sim N(0, \Sigma_0)$).

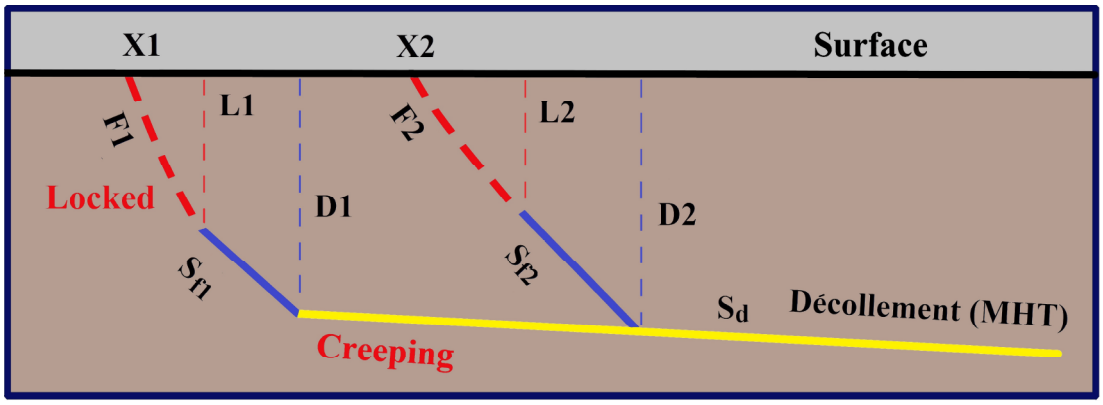

Fig. 4.4: Sketched map of the two-dimensional fault model. F1, Fault-1; F2, Fault-2; X1, Surface location of Fault-1; X2, Surface location of Fault-2; L1, Locking depth-1; L2, Locking depth-2; D1, Depth-1; D2, Depth-2; Sf1, Slip rate of Fault-1; Sf2, Slip rate of Fault-2, Sd, Slip rate detachment.

Further, a Bayesian inversion framework is implemented from Fukuda and Johnson (2008) [83] to estimate the fault slip distribution and other fault parameters. The Bayesian slip inversion model overcomes several deficiencies (e.g., slip inversion with unknown fault kinematics, choice of a-priori information of fault geometry, and others) of the previous slip-rate estimation techniques, such as the optimization formulation of inversion [66, 120], cross-validation method [300], and the application of ABIC (Akaike-Bayesian Information Criterion) [314] in inversion [83]. In the implementation of the Bayesian inversion for the observed geodetic data to deduce fault parameters, a simple Jeffreys prior (Gaussian distribution of known variance) is used depending on the possible range of the model parameters [19]. Guided by the geological studies on fault parameters, a-priori upper and lower bounds are defined for each parameter, outside of which the prior is considered to be zero [19].

In a Bayesian approach, the posterior distribution (i.e., $P(s, \sigma^2, m|d)$) of unknown parameters is determined from several repetitions of prior information (i.e., $P(s, m, \sigma^2)$)

based on how well the parameter knowledge can fit the observed data (likelihood function). Mathematically, the posterior distribution is represented as

$$P(s,\sigma^2,m|d) = \frac{p(d|s,m,\sigma^2) \times p(s,m,\sigma^2)}{\int_{-\infty}^{\infty} p(d|s,m,\sigma^2) \times p(s,m,\sigma^2)\, dm\, ds\, d\sigma^2} \tag{4.2}$$

As the integration part in the denominator of Equation (4.2) is independent to the unknown parameters, the posterior distribution is proportional to the multiplication of the likelihood function and the prior information.

$$P(s,\sigma^2,m|d) \propto p(d|s,m,\sigma^2) \times p(s,m,\sigma^2) \tag{4.3}$$

The likelihood function ($p(d|s,m,\sigma^2)$), that is defined based on the observed geodetic data for a given fault-slip, follows a normal distribution with mean $G(m) \times s$ and covariance matrix $\sigma^2\Sigma_0$. In the present analysis, for the regularization of Bayesian inversion, a-priori information of the fault parameters is constrained based on the available geological studies [e.g., 118, 140, 223, 283, 305, 321]. To estimate the joint posterior distribution of fault parameters and fault slip, a Markov Chain Monte Carlo (MCMC) method is employed incorporating the Metropolis algorithm [83]. A MATLAB code is developed to simulate the MCMC chain of samples from prior and likelihood. There are 10^6 iterations for each of the parameters in the posterior distribution. Among these iterations, first 'n' ($\sim$10% to 20% of the total number of iterations) values that constitute burn-in samples are removed from the final estimation [10, 19, 278]. These 'burn-in' samples constitute primary values, which are often influenced by the initial coarse guesses of the model parameters [10, 19, 278]. After removing burn-in samples, mean and standard deviation of the model parameters are computed [83]. The estimates of parameters can be represented by the statistical representation of their posterior distributions (Appendix A). The posterior probability distributions for the fault slip rate are depicted in Fig. 4.5 to Fig. 4.7. In the following sections, the modeling results are described for each of the fifteen transects (A-A' to O-O') (Fig. 4.8, Fig. 4.9, and Fig. 4.10).

4.4 Modeling results

The modeling results are presented separately for the northwest, central, and the northeast Himalaya in the sections below.

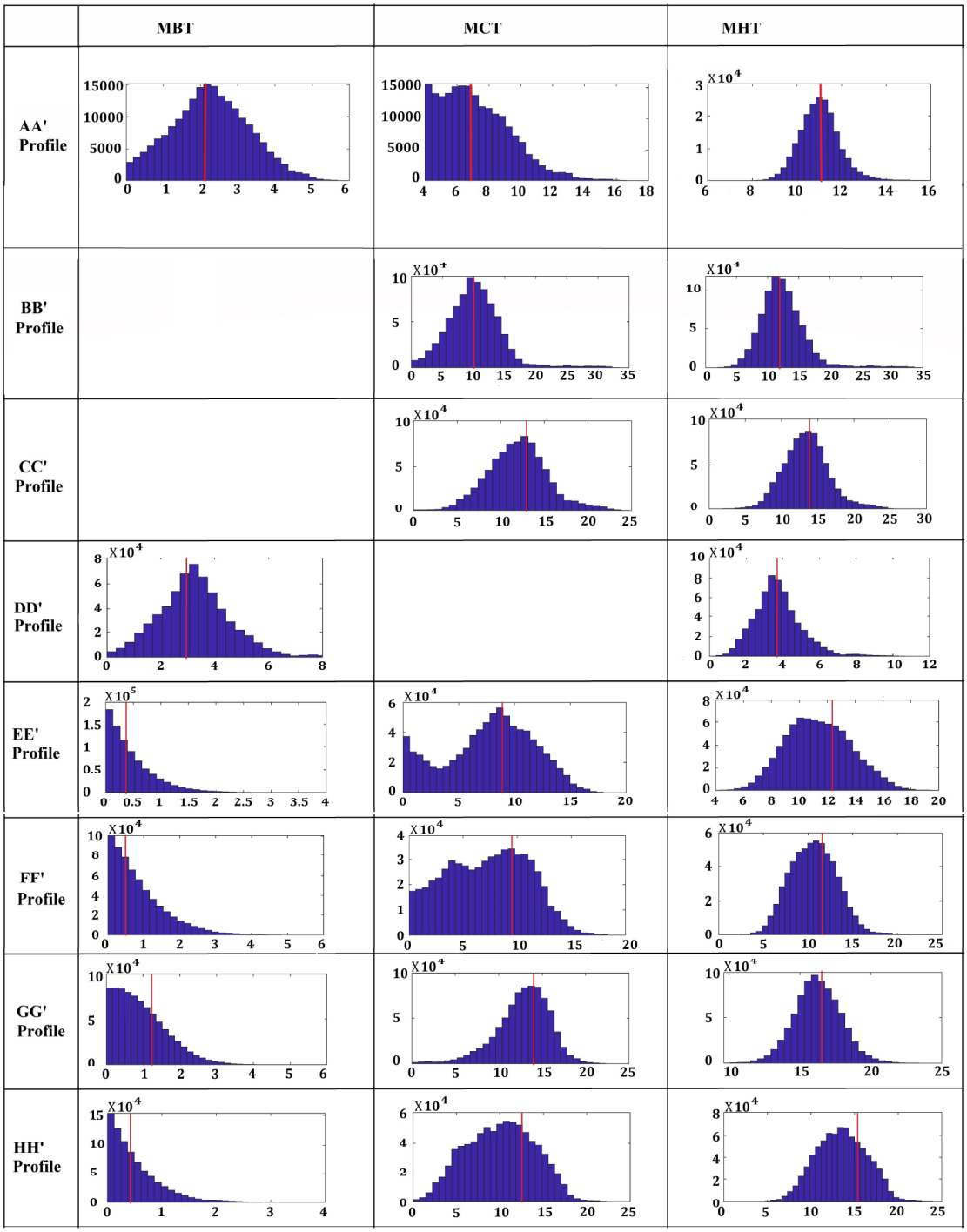

Fig. 4.5: Posterior probability distributions of slip rates of the major thrusts from the Bayesian inversion model along the northwest Himalaya. The red vertical lines show the mean values in the posterior distribution. The empty space in the rows represents that the above indicated fault is either not considered or not covered in the respective transect.

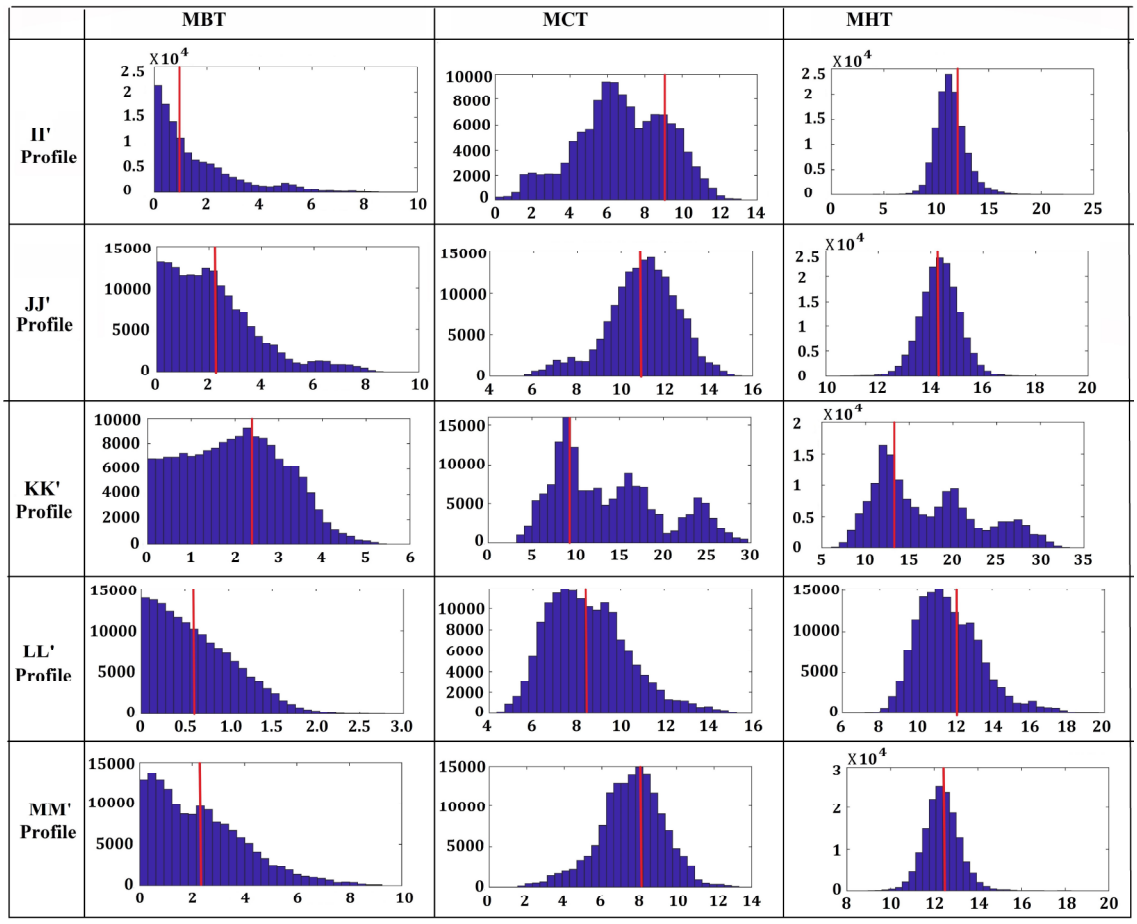

Fig. 4.6: Posterior probability distributions of slip rates of the major thrusts from the Bayesian inversion model along the central Himalaya. The red vertical lines show the mean values in the posterior distribution.

In Fig. 4.8 to Fig. 4.10, the uppermost panel shows elevation of the topography (in meters) along these profiles; the two middle panels represent fault-normal and fault-parallel components of the horizontal velocity; the last panel indicates geometries and slip rates on the faults; the light red and the light blue circles with error bars in the fault-normal and fault-parallel components denote surface velocities, whereas the black stars indicate modeled velocities; the red and blue dashed lines indicate model fitting; the vertical black dashed lines denote surface locations of the faults; and in the fault geometry panel, the dotted blue lines indicate fault locking.

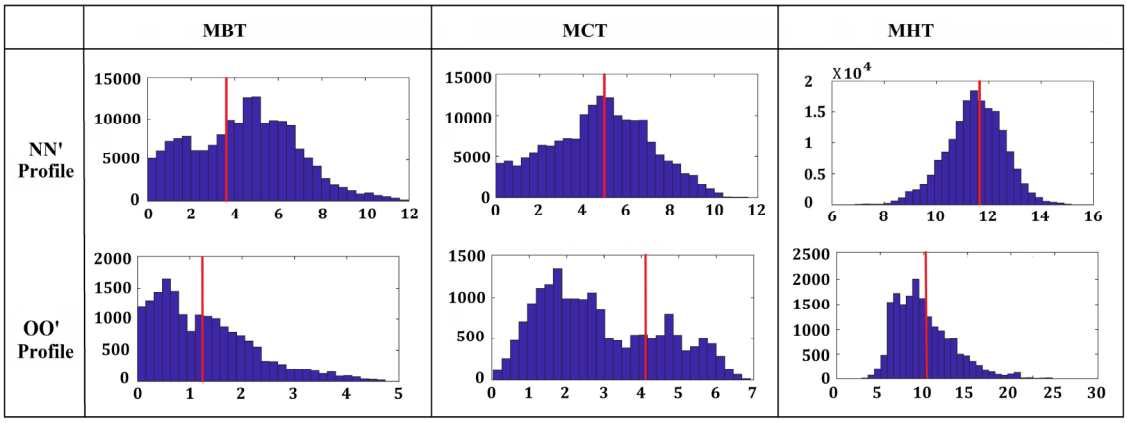

Fig. 4.7: Posterior probability distributions of slip rates of the major thrusts from the Bayesian inversion model along the northeast Himalaya. The red vertical lines show the mean values in the posterior distribution.

4.4.1 Modeling results along the northwest Himalaya

There are eight profiles (A-A' to H-H') in the northwest Himalaya. Fig. 4.8 presents the traces of eight GPS velocity profiles across the thrust system in the northwest Himalaya. In Fig. 4.8, horizontal GPS velocities, projected along the normal and parallel to the profile (A-A'−H-H'), are plotted together with the modeled velocities. In the fault-normal component, positive values indicate shortening and negative values indicate extension, whereas in the fault-parallel component, positive values show right-lateral motion and negative values indicate left-lateral motion of the fault.

In profile A-A', an insignificant slip rate (1.8±1.8 mm/yr) is observed for the MFT. Fault-parallel competent shows a small right lateral motion throughout the profile. As MBT and MCT are very close in this region, only the MCT is considered for the modeling purpose. Slip rates of the MCT and the MHT are 10±1 mm/yr and 10±1.2 mm/yr, receptively (Fig. 4.8 and Table 4.2).

The B-B' transect in the westernmost Himachal Himalaya shows insignificant fault slip across the MFT (Table 4.2). Similarly, a negligible shortening is obtained between the MFT and the JMT. The fault-parallel component indicates no notable velocity gradient, implying that the convergence around this region is mostly arc-normal (Fig. 4.8). As MCT and MBT lie very close to each other in the B-B' segment, the MCT alone is modeled. The modeling results suggest ∼10.0 mm/yr slip rate for ∼22° dipping MCT in the N-E direction (Fig. 4.8) and ∼12.3 mm/yr slip rate for the gently dipping décollement (MHT)(Fig. 4.8) and Table 4.2).

In the profile C-C', the MFT remains locked with a fault slip rate of ∼0.7 mm/yr (Table 4.2). The fault-normal component reveals only crustal shortening, whereas the fault-parallel component shows minor right-lateral motion below the MCT and a significant left-lateral motion above the MCT (Fig. 4.8). The slip rates of MCT and MHT in the C-C' profile are about 32% and 18% higher than that of the B-B' transect (Table 4.2).

The D-D' transect in the easternmost Himachal Himalaya reveals minor extension throughout the profile (Fig. 4.8). The MFT, with an estimated slip rate of ∼0.3 mm/yr, remains fully locked in this profile. A minor right-lateral strike-slip component (∼3 mm/yr) is observed in the fault-parallel section (Fig. 4.8). Due to the absence of GPS stations across the MCT, the slip rate contribution from other faults (i.e., MFT, MBT, and MHT) in the total slip of MHT is relatively small (∼3.8 mm/yr) (Fig. 4.8 and Table 4.2). In fact, due to the sparse resolution of GPS coverage in this area, it is difficult to provide any stringent evidence of localized deformation along the D-D' transect.

In the E-E' profile along the Dehradun valley, the MFT (∼0.4 mm/yr) shows a similar locking behavior, as evident in the earlier transects (Fig. 4.8 and Table 4.2). The fault slip rate (∼0.4 mm/yr) of MBT is also observed to be insignificant. However, at a profile distance of ∼100 km, a noteworthy velocity offset of ∼8.0 mm/yr in fault-normal section along with a strike-slip component of ∼3.5 mm/yr in fault-parallel part is observed (Fig. 4.8). Consequently, the slip rates for the MCT-I and the MHT are estimated as ∼12.9 mm/yr and ∼9.5 mm/yr, respectively (Table 4.2).

The results of fault kinematics in profile F-F' are comparable with that of transect E-E' (Fig. 4.8 and Table 4.2). In the F-F' transect, the frontal thrust (i.e., MFT) is also observed to be persistently locked. The fault-parallel component reveals right-lateral motion along the profile with a maximum rate of ∼2.0 mm/yr near the surface trace of the Tons Thrust (TT) fault. Overall, ∼10.0 mm/yr of shortening is observed in this profile (Fig. 4.8). Both fault-normal and fault-parallel components of the F-F' profile show a similar pattern of crustal behavior (shortening and left-lateral motion) with that of the E-E' profile. Similarly, a comparable fault-slip (∼9.8 mm/yr) for MCT-I in the F-F' transect is also observed (Table 4.2).

The G-G' transect is defined along the western part of the Kumaun Himalaya. Both MFT and MBT are locked in this profile with slip rates of ∼0.6 mm/yr and ∼1.1 mm/yr, respectively. A significant velocity gradient is located across the location of ∼160 km (Fig. 4.8) in the fault-normal component. This results in a slip rate of ∼13.8 mm/yr for the MCT-I (Table 4.2). A significant strike-slip offset (∼4.5 mm/yr) is observed across

the surface location of ∼160 km in the fault-parallel component (Fig. 4.8). In addition, the slip rate (∼17.0 mm/yr) of MHT in this transect turns out to be the highest among all transects.

In profile H-H', MFT and MBT are observed to be locked with their slip rates ∼0.2 mm/yr and ∼0.5 mm/yr, respectively (Table 4.2). While the fault-normal component reveals mostly contraction (∼10 mm/yr), the fault-parallel component shows significant left-lateral motion (∼6 mm/yr). The MCT-I in this profile indicates the oblique motion of ∼12.5 mm/yr in the N-E direction. Nonetheless, estimated geometric fault parameters for all fault segments in both profiles (G-G' and H-H') are observed to be consistent (Fig. 4.8). A slip rate of ∼15.5 mm/yr for MHT is also obtained in this profile.

The modeling results along the northwest Himalaya are displayed in Fig. 4.8 and summarized in Table 4.2.

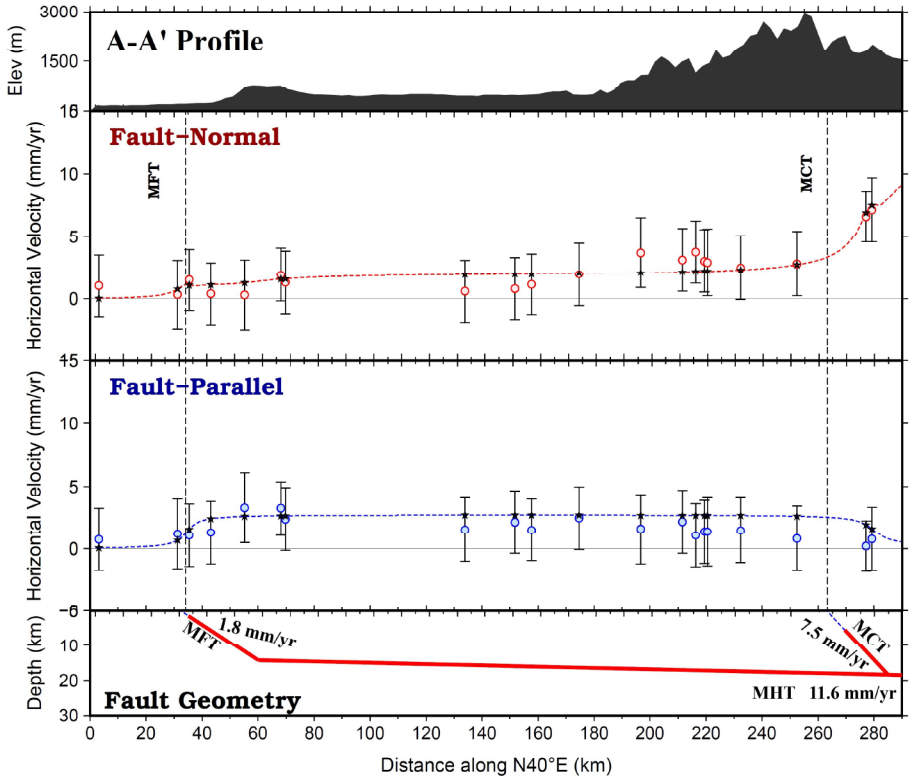

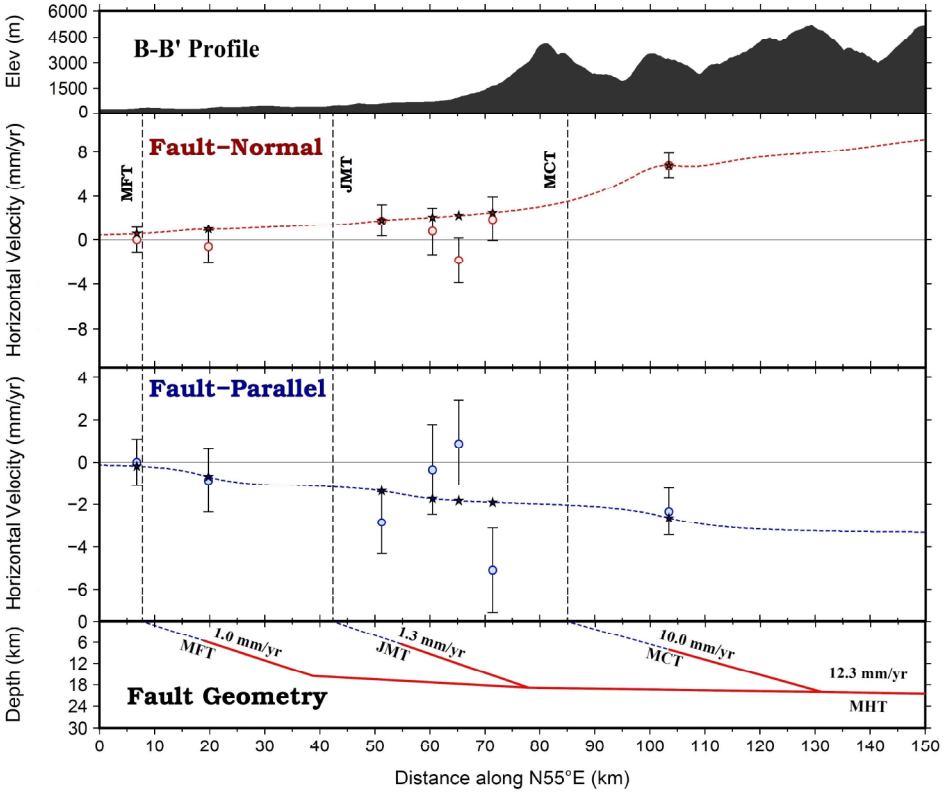
B-B' Profile
Elev (m)
Fault-Normal
Fault-Parallel
Horizontal Velocity (mm/yr)
MFT
JMT
MCT
Depth (km)
1.0 mm/yr
1.3 mm/yr
10.0 mm/yr
12.3 mm/yr
MHT
Fault Geometry
Distance along N55°E (km)

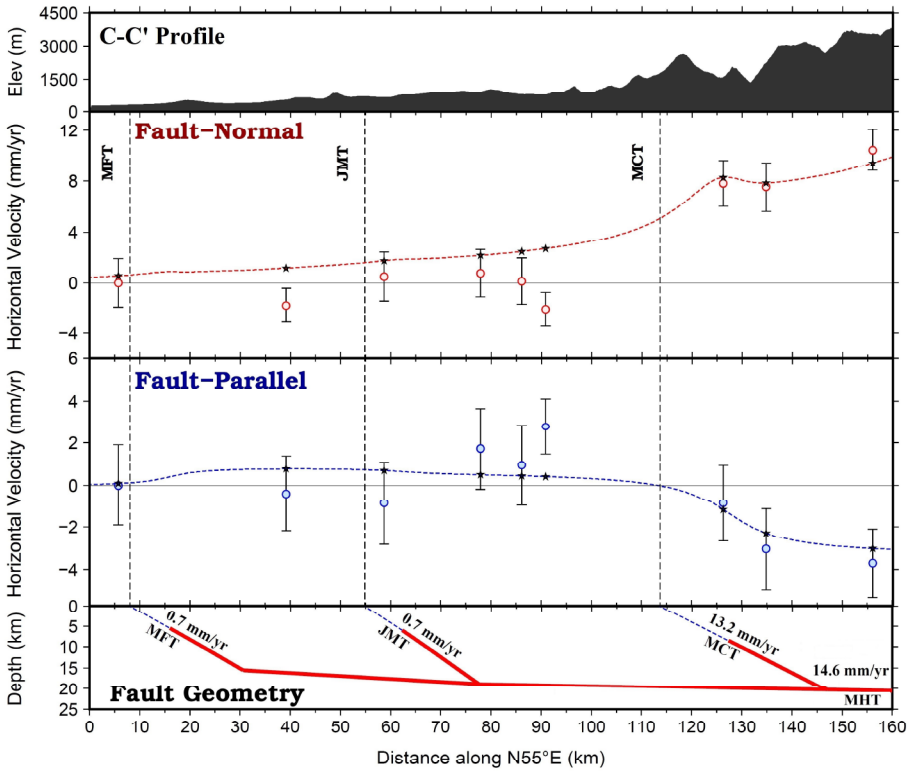
C-C' Profile
Elev (m)
Fault-Normal
Fault-Parallel
Horizontal Velocity (mm/yr)
MFT
JMT
MCT
Depth (km)
0.7 mm/yr
0.7 mm/yr
13.2 mm/yr
14.6 mm/yr
MHT
Fault Geometry
Distance along N55°E (km)

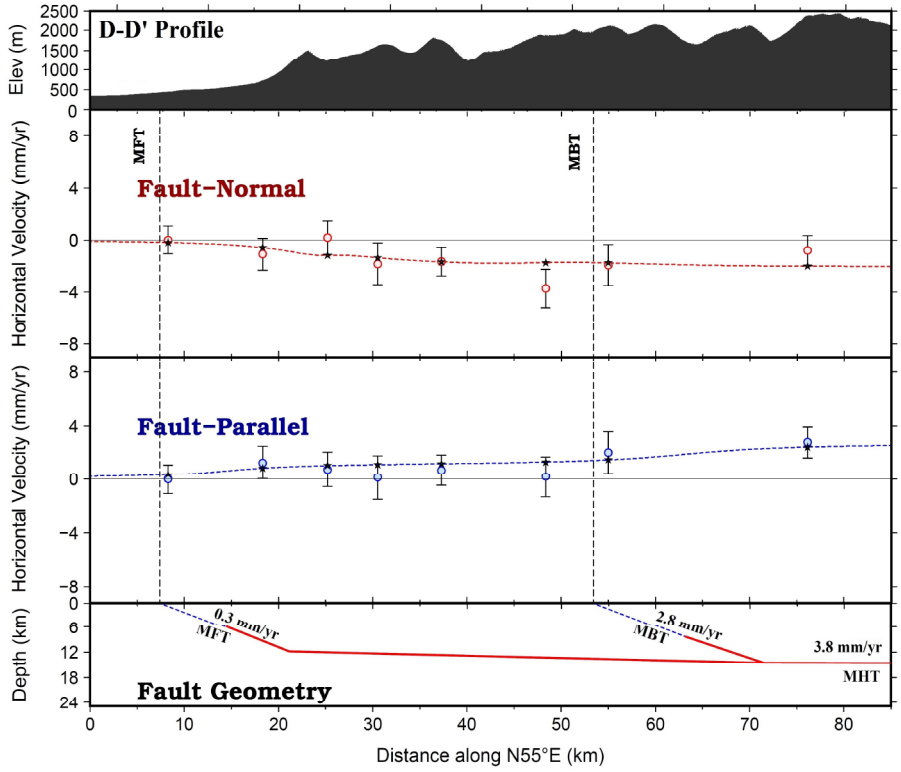
D-D' Profile
Elev (m)
Fault-Normal
Fault-Parallel
Horizontal Velocity (mm/yr)
MFT
MBT
Depth (km)
0.3 mm/yr
2.8 mm/yr
3.8 mm/yr
MHT
Fault Geometry
Distance along N55°E (km)

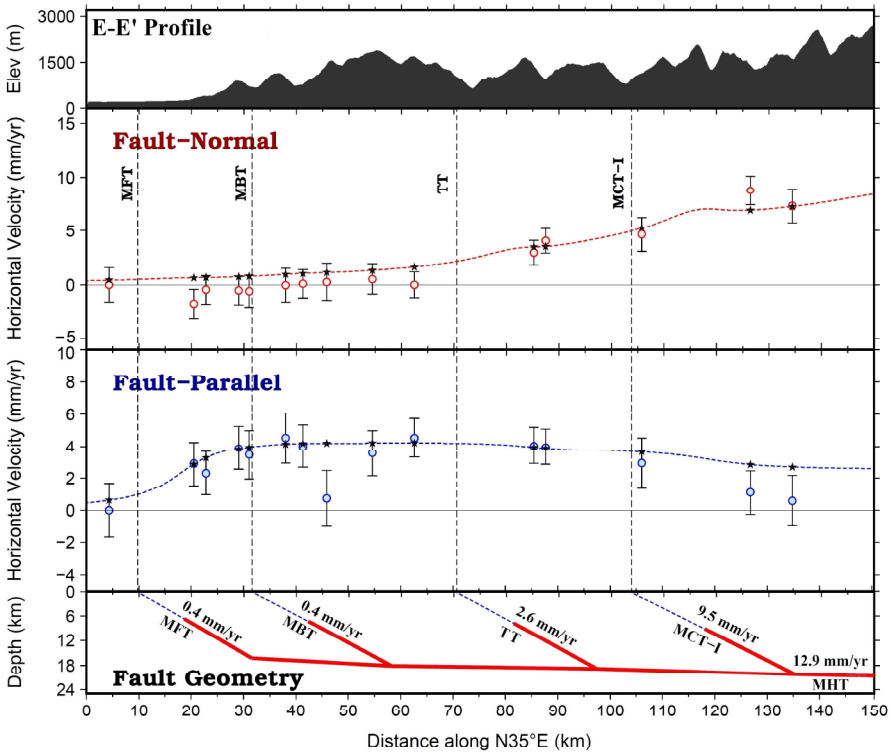
E-E' Profile
Elev (m)
Fault-Normal
Fault-Parallel
Horizontal Velocity (mm/yr)
MFT
MBT
TT
MCT-I
Depth (km)
0.4 mm/yr
0.4 mm/yr
2.6 mm/yr
9.5 mm/yr
12.9 mm/yr
MHT
Fault Geometry
Distance along N35°E (km)

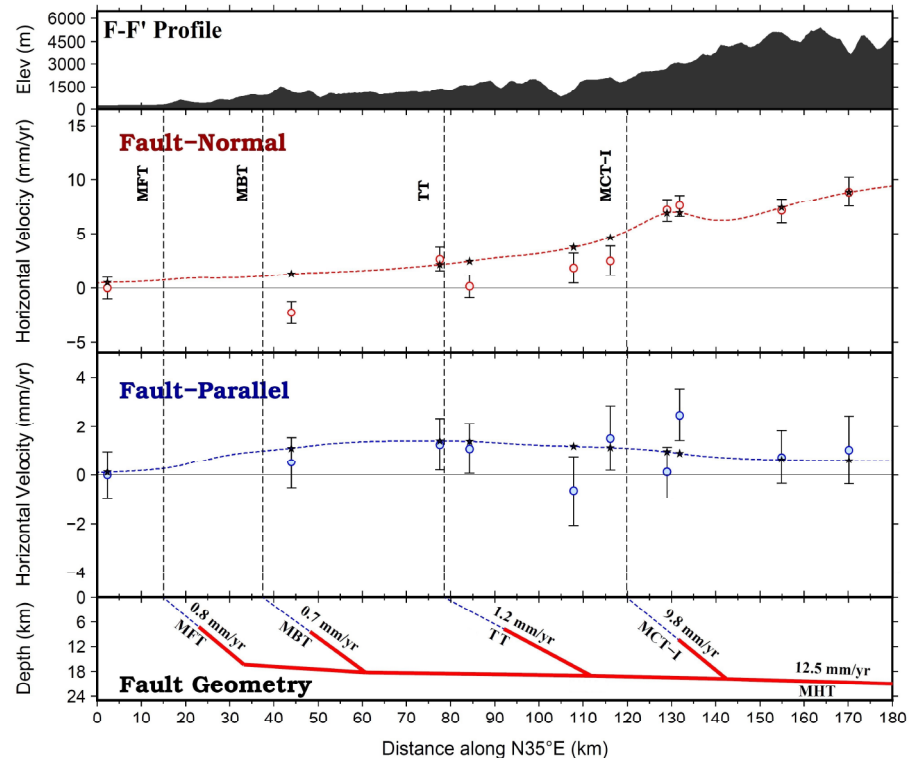
F-F' Profile
Elev (m)
Fault-Normal
Horizontal Velocity (mm/yr)
MFT
MBT
TT
MCT-I
Fault-Parallel
Horizontal Velocity (mm/yr)
Depth (km)
0.8 mm/yr
MFT
0.7 mm/yr
MBT
1.2 mm/yr
TT
9.8 mm/yr
MCT-I
12.5 mm/yr
MHT
Fault Geometry
Distance along N35°E (km)

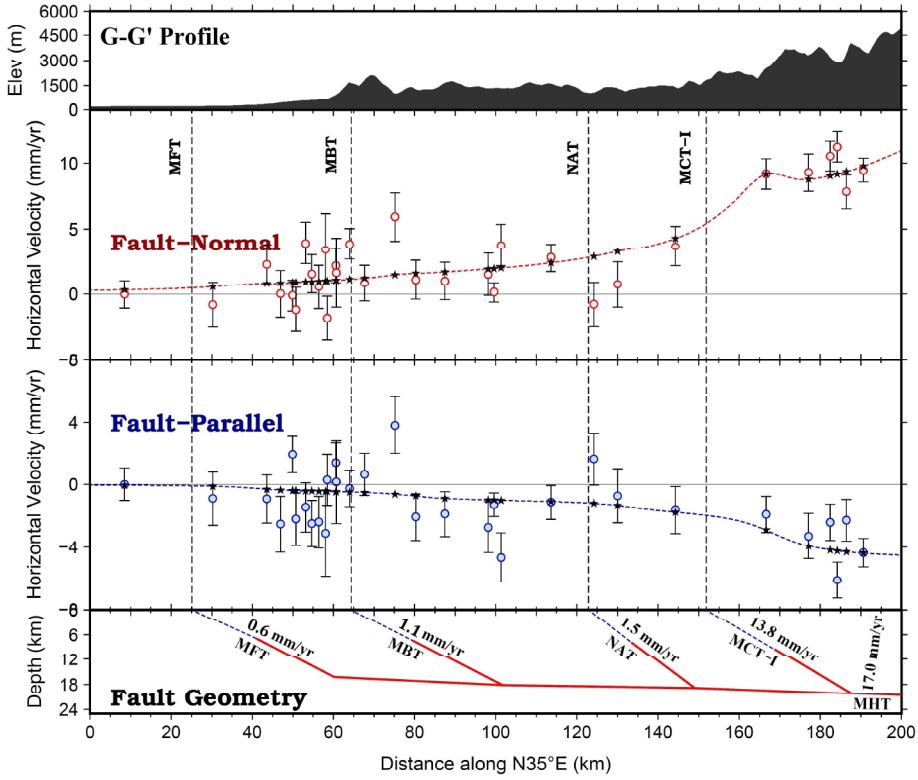
G-G' Profile
Elev (m)
Fault-Normal
Horizontal Velocity (mm/yr)
MFT
MBT
NAT
MCT-I
Fault-Parallel
Horizontal Velocity (mm/yr)
Depth (km)
0.6 mm/yr
MFT
1.1 mm/yr
MBT
1.5 mm/yr
NAT
13.8 mm/yr
MCT-I
17.0 mm/yr
MHT
Fault Geometry
Distance along N35°E (km)

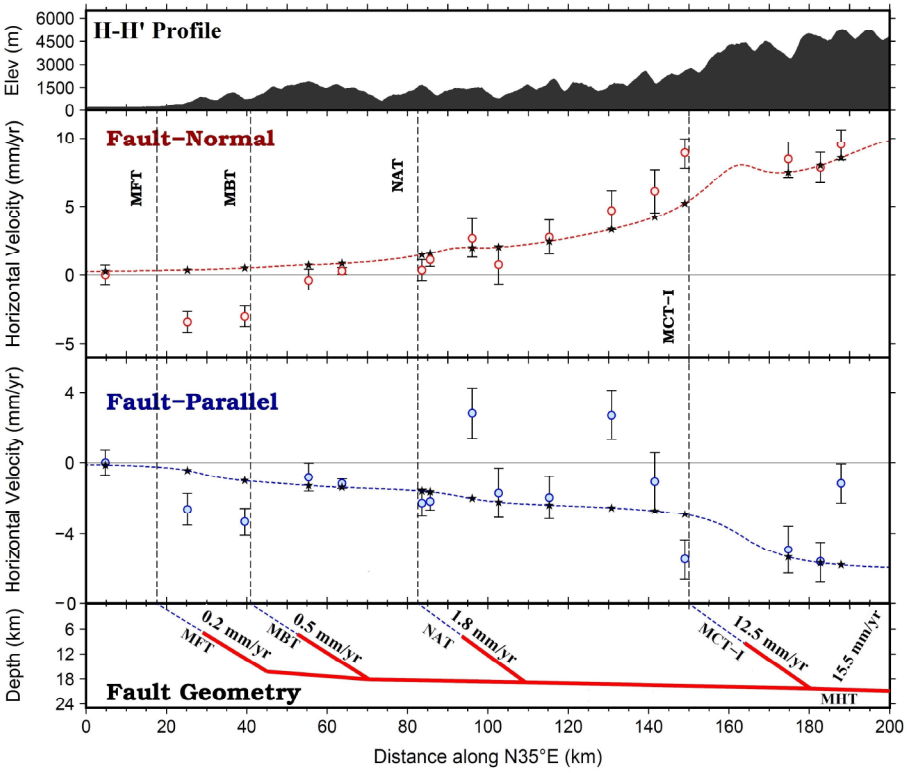

Fig. 4.8: Modeling results across eight profiles (A-A' to H-H') along the northwest Himalaya.

Table 4.2: Modeled fault parameters along eight transects of the northwest Himalaya. The dashed line in the table indicates that no fault parameter is available.

Transect	Fault	Dip (°)	Depth (km)	Locking Depth (km)	Surface Location (km)	Rake (°)	Slip Rate (mm/yr)
A-A'	MFT	31±2	15±0.2	1.8±0.1	28.4±2.5	–	1.8±1.8
	MCT	35±1	22±0.9	5.4±0.7	263.3±3.5	109±4	7.5±0.5
	MHT	–	–	–	–	74±8	11.6±0.4
B-B'	MFT	27±4	15.5±0.3	5.5±0.3	7.8±1.4	–	1.0±2.6
	JMT	29±3	18.9±0.6	6.5±0.3	42.4±1.4	135±3	1.3±1.1
	MCT	22±4	20.1±0.5	8.0±0.6	85.0±1.6	99±3	10.0±1.6
	MHT	–	–	–	–	107±1	12.3±1.8

C-C'	MFT	35±4	15.5±0.3	5.5±0.3	8.0±0.6	–	0.7±2.0
	JMT	33±7	18.7±0.4	6.0±0.3	54.8±2.8	124±4	0.7±0.7
	MCT	31±4	20.3±0.4	8.5±0.3	113.6±4.0	114±3	13.2±1.3
	MHT	–	–	–	–	108±4	14.6±1.4
D-D'	MFT	35±1	11.8±0.5	6.0±0.9	7.4±1.2	–	0.3±0.9
	MCT	30±3	14.5±0.3	8.3±0.7	53.4±1.0	45±3	2.8±0.9
	MHT	–	–	–	–	9±5	3.8±0.9
E-E'	MFT	37±1	16.1±0.4	6.5±0.8	9.9±0.8	–	0.4±1.0
	MBT	32±1	17.9±0.3	7.0±0.7	30.8±1.2	50±1	0.4±0.3
	TT	32±1	19.0±0.4	7.7±0.4	67.1±0.7	103±1	2.6±0.5
	MCT-I	34±1	20.5±0.4	8.9±0.4	104.0±0.6	115±1	9.5±0.5
	MHT	–	–	–	–	85±1	12.9±0.7
F-F'	MFT	40±2	16.1±0.4	7.1±0.4	15.0±1.2	–	0.8±2.2
	MBT	28±4	18.2±0.4	8.4±0.7	37.5±0.7	45±4	0.7±0.6
	TT	30±2	19.0±0.4	7.7±0.4	78.6±0.9	105±2	1.2±0.9
	MCT-I	35±2	19.8±0.4	10.3±0.5	119.8±0.9	105±2	9.8±1.5
	MHT	–	–	–	–	84±2	12.5±1.1
G-G'	MFT	25±1	16.3±0.4	6.8±0.7	25.1±1.4	–	0.6±2.5
	MBT	33±2	18.2±0.4	8.2±0.9	64.4±1.0	123±5	1.1±0.6
	NAT	37±1	18.9±0.4	7.8±0.4	122.9±1.1	117±6	1.5±0.8
	MCT-I	24±2	20.4±0.7	9.3±0.8	151.9±2.2	117±6	13.8±1.8
	MHT	–	–	–	–	107±1	17.0±1.8
H-H'	MFT	31±5	16.3±0.4	6.8±0.7	17.6±1.4	–	0.2±2.5
	MBT	31±8	18.2±0.4	7.2±1.2	40.9±2.0	115±13	0.5±0.4
	NAT	36±4	18.9±0.7	7.7±0.4	82.3±1.5	110±1	1.8±1.2
	MCT-I	34±7	20.3±0.7	9.3±0.9	149.7±2.9	107±8	12.5±1.2
	MHT	–	–	–	–	113±7	15.5±1.6

4.4.2 Modeling results along the central Himalaya

There are five profiles (I-I' to M-M') in the central Himalaya. The estimated slip rates (1.8±1.8 to 1.9±1.0 mm/yr and 2.3±0.7 to 2.3±0.3 mm/yr) of the MFT and the MBT

along these transects (I-I' to M-M') are very small, indicating fault coupling mechanism throughout the central Himalaya (Table 4.3). Fault-normal and fault-parallel components along the profiles J-J' to M-M' show identical patterns, indicating comparable slip rate and fault-geometry throughout these transects. In I-I' profile, a small right lateral motion is observed from the southernmost point of the transect up to the MBT. In the north of the MBT, a continuous right lateral motion of about ∼5 mm/yr is observed (Fig. 4.9). It may be noted that the left lateral motion in transect H-H' and the region between profiles H-H' and I-I' could be a transition zone from the left lateral to the right lateral motion (Fig. 4.9 and Fig. 4.9). In transect J-J' to M-M', a significant change in the fault-parallel component is observed in the north of the MCT. All transects (J-J' to M-M') show ∼10 mm/yr of right lateral motion (Fig. 4.9). A major change in dextral motion (north to the MCT) indicates the possible impact of extension of the Tibetan Plateau in an east-west direction. The Plateau is known to be extending rightward in the southeast (central to northeast Himalaya) and leftward in the west (northwest Himalaya) [72, 73]. The slip rates of MCT and MHT range between 7.5±0.5 mm/yr and 11.0±1.6 mm/yr and between 11.6±0.4 mm/yr and 14.4±1.8 mm/yr, respectively along the central Himalaya (transect I-I' to M-M') (Fig. 4.9 and Table 4.3). The other fault geometries (dip angle, depth, locking depth, and rake angle) along the whole central Himalaya (transect I-I' to M-M) are observed to be consistent for the megathrust system (Table 4.3). The modeling results along the central Himalaya are pictorially shown in Fig. 4.9 and summarized in Table 4.3.

Table 4.3: Modeled fault parameters along five transects in the central Himalaya. The dashed line in the table indicates that no fault parameter is available.

Transect	Fault	Dip (°)	Depth (km)	Locking Depth (km)	Surface Location (km)	Rake (°)	Slip Rate (mm/yr)
I-I'	MFT	20±2	17.8±0.2	3.3±0.1	25.3±2.5	–	1.8±1.8
	MBT	29±2	20.0±0.5	3.5±0.1	51.4±3.1	58±4	2.3±0.7
	MCT	26±3	22.5±0.9	3.7±0.7	113.6±3.5	82±8	7.5±0.5
	MHT	–	–	–	–	67±8	11.6±0.4

J-J'	MFT	21±2	14.2±0.3	4.1±0.3	20.4±1.4	–	1.2±2.6
	MBT	27±3	18.3±0.6	3.4±0.3	52.9±1.4	76±3	2.2±1.1
	MCT	28±5	22.6±0.5	3.5±0.6	106.5±1.6	56±3	11.0±1.6
	MHT	–	–	–	–	50±1	14.4±1.8
K-K'	MFT	22±6	12.7±0.3	3.9±0.3	32.3±0.6	–	1.9±2.0
	MBT	27±2	15.2±0.4	3.7±0.3	61.3±2.8	70±4	2.7±0.7
	MCT	28±1	20.4±0.4	4.0±0.3	135.1±4.0	63±3	9.9±1.3
	MHT	–	–	–	–	58±4	14.5±1.4
L-L'	MFT	27±4	14.3±0.5	3.9±0.9	27.7±1.2	–	2.8±3.0
	MBT	30±8	17.8±0.3	3.5±0.7	40.4±1.0	82±5	0.8±0.9
	MCT	29±9	22.0±0.4	3.7	117.6±1.4	55±3	8.5±0.9
	MHT	–	–	–	–	53±5	12.1±0.9
M-M'	MFT	28±1	13.6±0.4	3.9±0.8	23.5±0.8	–	1.9±1.0
	MBT	28±5	17.6±0.3	3.5±0.7	68.1±1.2	79±1	2.3±0.3
	MCT	28±2	22.2±0.4	3.7±0.4	99.8±0.6	52±1	8.4±0.5
	MHT	–	–	–	–	54±1	12.6±0.7

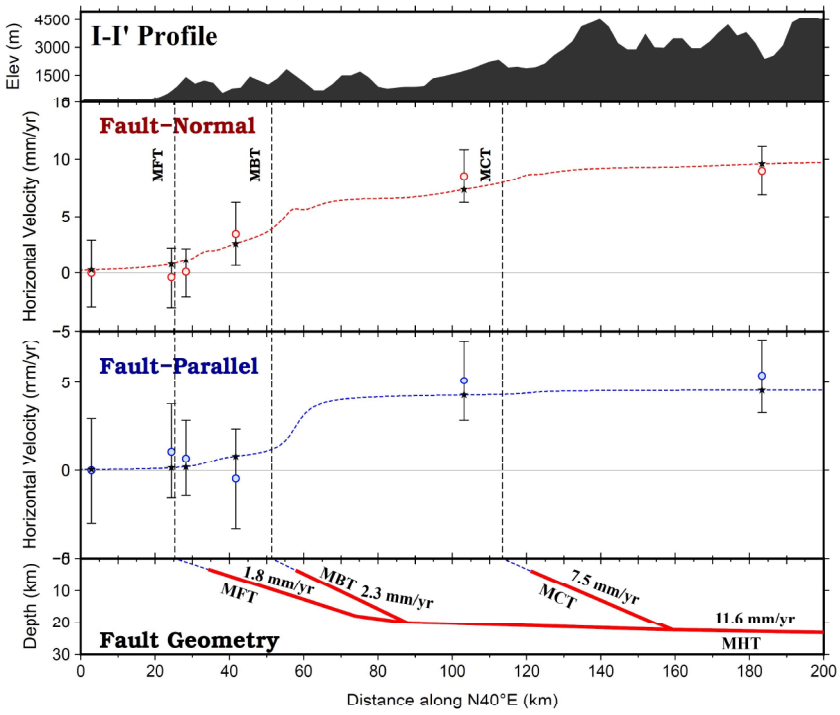

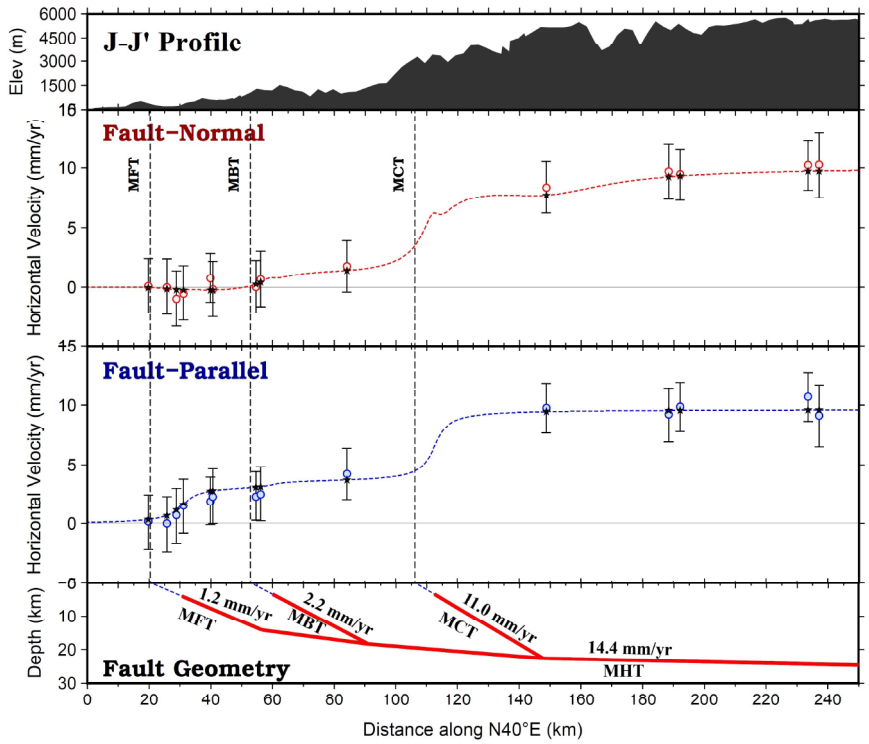
J-J' Profile
Elev (m)
Fault-Normal
Fault-Parallel
Horizontal Velocity (mm/yr)
MFT
MBT
MCT
Depth (km)
1.2 mm/yr
2.2 mm/yr
11.0 mm/yr
14.4 mm/yr
MHT
Fault Geometry
Distance along N40°E (km)

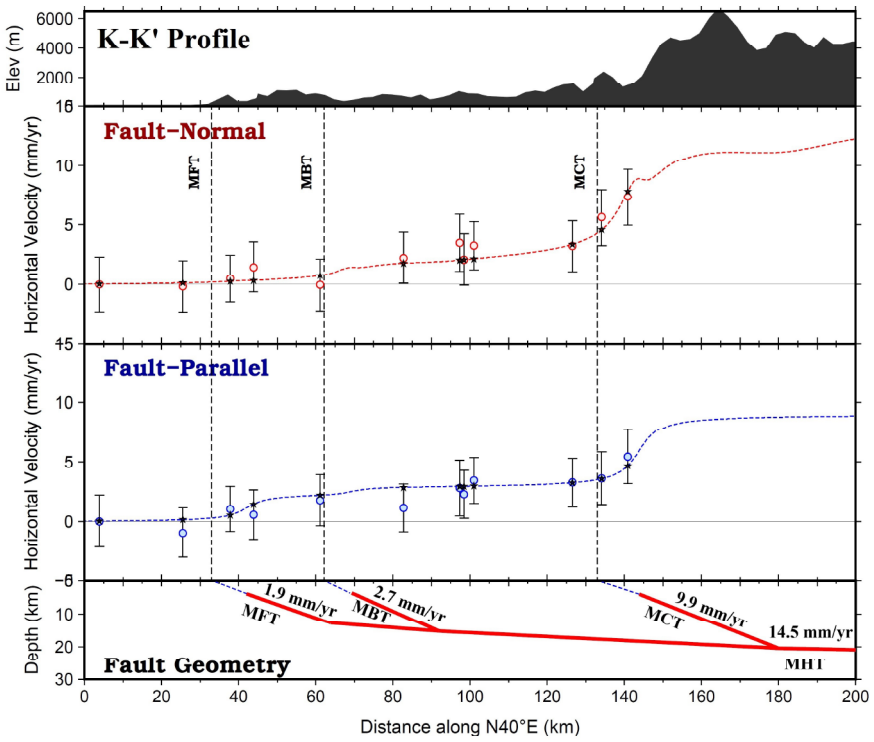
K-K' Profile
Elev (m)
Fault-Normal
Fault-Parallel
Horizontal Velocity (mm/yr)
MFT
MBT
MCT
Depth (km)
1.9 mm/yr
2.7 mm/yr
9.9 mm/yr
14.5 mm/yr
MHT
Fault Geometry
Distance along N40°E (km)

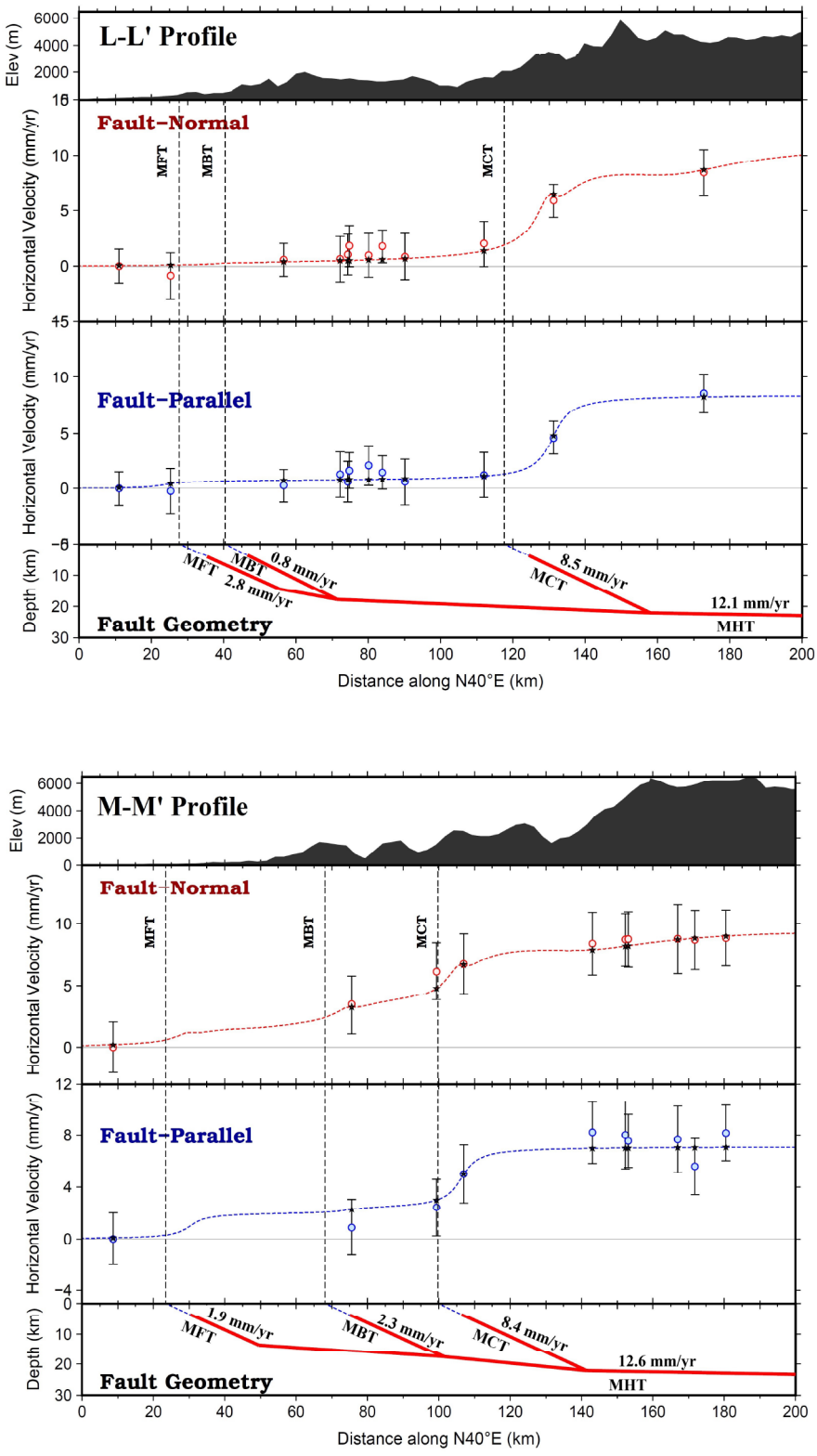

Fig. 4.9: Modeling results across five profiles in the central Himalaya.

4.4.3 Modeling results along the northeast Himalaya

There are two profiles (N-N' and O-O') in the northeast Himalaya. The reason for choosing these two profiles along the northeastern part of the Himalayan arc is that the surface velocity field resolution in this region is sparse and the available GPS velocity vectors do not cover the Himalayan megathrust system.

Clear distinctions in fault geometry are observed between the transects of the northeast Himalaya and the central Himalaya. The fault-parallel components are larger in both profiles in comparison to the fault-parallel components observed in the central Himalaya. Large dextral rates are estimated (>10 mm/yr) in these transects (Fig. 4.10). However, contraction rates along these transects are comparatively small. The large right lateral and smaller shortening rates in the northeast Himalaya indicate the impact of extension of the Tibetan Plateau and the YDR. Apart from this, small slip rates (2.7±1.8 mm/yr and 3.9±0.7 mm/yr in transect N-N', and 2.7±2.6 mm/yr and 1.3±1.1 mm/yr in transect O-O') are observed for both MFT and MBT along these profiles. This evidence suggests the progression of the locking behavior of these two faults, starting from the northwest Himalaya, continuing to the central Himalaya, and further extending up to the northeast Himalaya (Table 4.4). The slip rate (4.2±1.6 mm/yr to 5.2±0.5 mm/yr) of MCT is found to be smaller in the northeast Himalaya than the northwest and the central Himalaya. In contrast, the slip rate (∼11.6±1.8 mm/yr) of the MHT shows a consistent behavior throughout the entire Himalayan segment (Table 4.4). A smaller rake angle is observed in both transects of the northeast Himalaya than that of the other segments of the Himalaya (A-A' to M-M'). Modeling results along the northeast Himalaya are displayed in Fig. 4.10 and summarized in Table 4.4.

Table 4.4: Modeled fault parameters along two transects of the northeast Himalaya

Transect	Fault	Dip (°)	Depth (km)	Locking Depth (km)	Surface Location (km)	Rake (°)	Slip Rate (mm/yr)
N-N'	MFT	21±2	14.1±0.2	4.2±0.1	29.3±2.5	–	2.7±1.8
	MBT	22±2	18.4±0.5	3.9±0.1	45.0±3.1	32±4	3.9±0.7
	MCT	39±3	21.3±0.9	3.4±0.7	92.1±3.5	32±8	5.2±0.5
	MHT	–	–	–	–	20±8	11.8±0.4

O-O'	MFT	38±2	12.3±0.3	2.4±0.3	44.8±1.4	–	2.7±2.6
	MBT	32±3	15.1±0.6	3.9±0.3	58.6±1.4	24±3	1.3±1.1
	MCT	23±5	22.8±0.5	4.6±0.6	126.7±1.6	60±3	4.2±1.6
	MHT	–	–	–	–	30±1	11.2±1.8

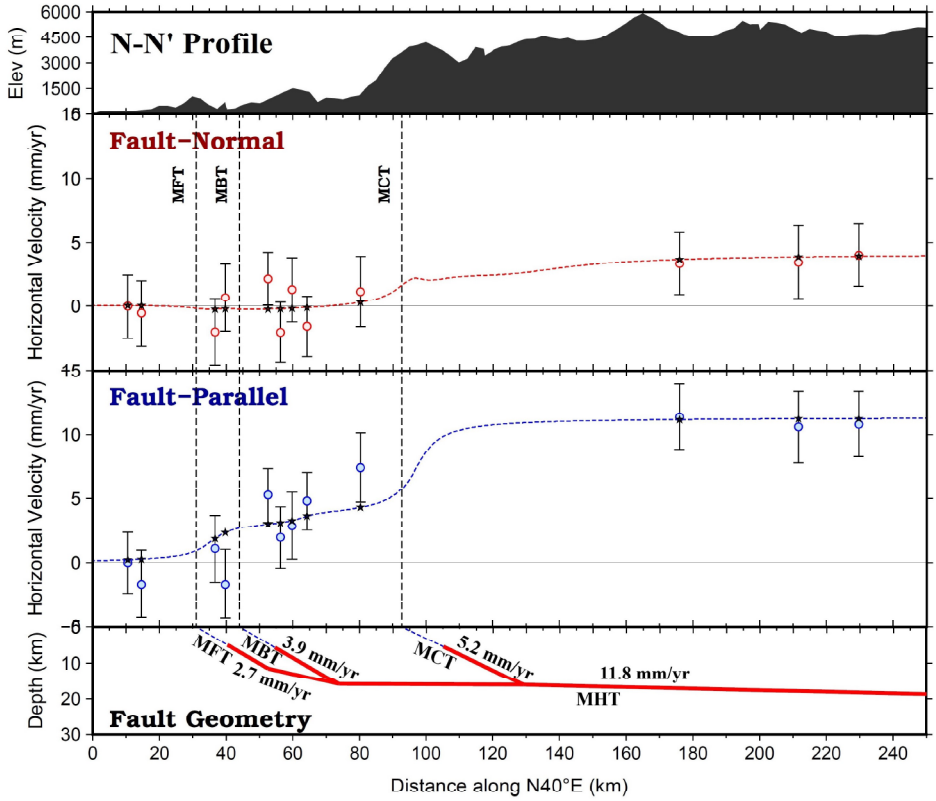

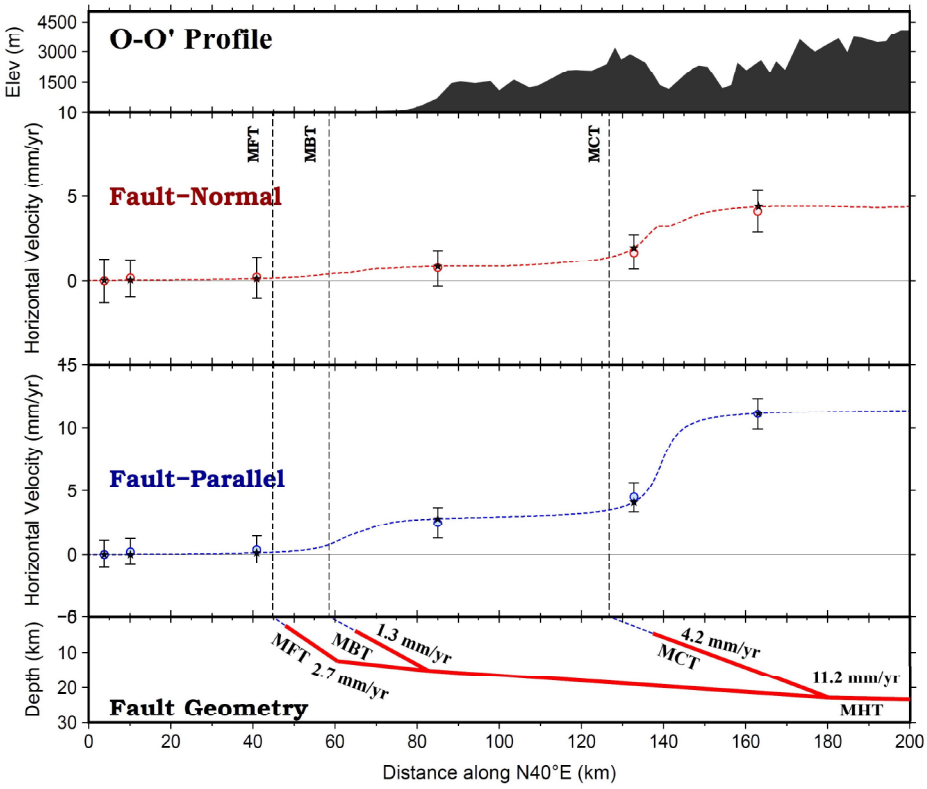

Fig. 4.10: Modeling results across two profiles in the northeast Himalaya.

4.5 Discussion

In this section, a detailed discussion of the modeling results is provided in terms of the along-strike slip rate distribution in the Himalayan arc, comparison of the proposed splay fault model with the conventional single fault model, and implication of the observed modeling results in seismic hazard assessment along the Himalayan arc.

4.5.1 Along-strike slip rate distribution of the Himalayan megathrust system

While a consistent slip rate (∼1.4 mm/yr) of MFT is obtained along the whole Himalayan arc, the slip rates of MBT and MCT range from ∼0.4 mm/yr to ∼3.9 mm/yr and ∼4.2 mm/yr to ∼13.8 mm/yr, respectively. This varying slip rate highlights the locked portions of MFT and MBT along which future earthquakes might strike [e.g., 17, 54, 277].

It may be noted that most of the previous geodetic studies [20, 62, 152, 154, 219, 221, 272, 277, 316] in the Himalaya have considered a "single fault model" for crustal

deformation analysis. This means that they have considered the contribution of the MHT alone, along with its surface manifestation fault (i.e., MFT) to analyze the present-day crustal deformation [20, 154, 219]. Such a model assumes that large earthquakes have occurred along the mid-crustal ramp and shallow décollement of the MHT, whereas the MCT remains dormant in the interseismic period [277]. In contrast to the above studies, the observed slip rate of MCT in the present study reveals its active behavior. This observation agrees to the studies by Mukhopadhyay (2011) [184] and Mridula et al. (2016) [177] who have found clusters of moderate size earthquakes around the MCT zone.

One of the primary results of this chapter is the slip rate of the MHT and its partitioning behavior along the Himalaya. The modeling results (Section 4.4) suggest the presence of first-order along-strike variation in the fault-slip rate of the MHT ($\sim$11.2$\pm$1.8 mm/yr to $\sim$17.0$\pm$1.8 mm/yr) from A-A' to O-O' profiles along the Himalayan arc. The average slip rate of the MHT is obtained as $\sim$13.8$\pm$3.1 mm/yr (excluding the slip rate of MHT from the D-D' profile where there is no data coverage across MCT), $\sim$13.1$\pm$1.8 mm/yr, and $\sim$11.5$\pm$1.8 mm/yr along the northwest, central, and the northeast Himalaya, respectively. This estimated slip rate of the MHT is $\sim$23%, $\sim$34%, and $\sim$40% lesser than that of Stevens and Avouac (2015) [277] along the northwest, central, and the northeast Himalaya, respectively. They have used an optimization inversion technique (i.e., reduced chi-square criterion) in their analysis [277], whereas the present analysis considers a fully Bayesian inversion approach. In particular, the estimated slip rate of the MHT in Garhwal (E-E' and F-F' profile) ($\sim$12.7$\pm$1.3 mm/yr) and Kumaun (G-G' and H-H' profile) ($\sim$16.3$\pm$3.4 mm/yr) region is observed to be $\sim$21% and $\sim$11% lesser, respectively, from the slip rates estimated by Jade et al. (2014) [114]. Similarly, the calculated slip rate of the MHT ($\sim$14.8$\pm$2.6 mm/yr) along the entire Garhwal-Kumaun region is about 20% lower than that of Yadav et al. (2019) [316]. The slip rate of the MHT in the present analysis is consistent ($\sim$ 7% and $\sim$3%) along the northwest and central Himalaya, and $\sim$28% lesser in the northeast Himalaya to the estimated slip rate of Lindsey et al. (2018) [154]. In addition, the calculated fault-slip rate for MHT ($\sim$17.0$\pm$1.4 mm/yr) in the Kumaun Himalaya (G-G' profile) closely agrees to the recent estimation of 17.2 $\pm$1.0 mm/yr by Ponraj et al. (2019) [219]. The above discrepancies in the slip rate estimation of the MHT are possibly because of three reasons: (i) the GPS data resolution in the present analysis is much higher than the previous studies; (ii) the inversion approach is based on a fully Bayesian framework [10, 83, 278], which inherently overcomes several limitations (e.g.,

subjective choice of Laplacian smoothing factor) of the traditional optimization inversion techniques used in the above studies [114, 154, 219, 277, 316]; and (iii) moreover, a splay fault model (multi-fault model) was used to consider the contribution from all major faults within the transects, rather than a single fault model.

4.5.2 Comparison of splay fault model and single fault model

In order to verify whether the estimated fault kinematics of the décollement from the proposed splay-fault model is similar to that of a single fault model [114, 154, 219, 277, 316], a single fault model is also implemented for all 15 transects (A-A' to O-O'). A brief comparison of the findings from splay-fault model and single-fault model along the northwest Himalaya, central Himalaya, and the northeast Himalaya is discussed below.

The slip rate of the MFT in A-A' profile is similar in both models (splay and single fault), though the slip rate of the MHT from the single fault model is ∼25% lesser than that of the splay fault model. The slip rates of the MFT and the MHT from the single fault model are about 50% higher in the B-B' profile. In C-C' profile, fault-parallel component shows a similar pattern, though a small extension (∼2 mm/yr) in the fault-normal component between the profile distance of 10 km and 90 km is observed in the single fault model. The slip rates of the MFT and the MHT in the C-C' profile are about ∼64% and ∼33% higher than the splay fault model. The slip rates of the MFT and the MHT in the D-D' profile are very high in the single fault model. As mentioned before, the slip rate of the MHT from the splay fault model is the sum of the slip rates of its splaying faults (i.e., MFT, MBT, and MCT). Due to this reason, the slip rate of the MHT (3.8 ± 0.9) in the D-D' transect is much smaller (as the MCT is not covered in this transect) than other transects in the splay fault model. However, in the single fault model, the slip rate of the décollement does not depend on its splay fault, and as a result, the slip rate of the MHT is higher (19.8 ± 1.5) in the D-D' transect. Further, in the profile E-E', the fault-normal component in both models shows consistent behavior, though, in the fault-parallel component of the single fault model, the strike-slip motion changes from right lateral to left lateral at a profile distance of ∼135 km. A similar change in the fault-parallel component in the single fault model is also evident in the F-F' profile. The slip rates of the MFT in both profiles (E-E' and F-F') are similar and about 70% higher than that of the splay fault model. However, the slip rate of the MHT in the E-E' is 42% higher and only 16% higher in the F-F' profile than that of the splay fault model. In the profile G-G' and H-H', a similar model fitting is observed in both the models, whereas the slip

rates of the MHT in these profiles are about >10% higher than that of the splay fault model.

The model fitting in the single fault model along all the profiles (I-I' to M-M') of the central Himalaya is consistent with that of the splay fault model. The slip rate of MHT is observed as: ∼25% higher in I-I' profile, ∼6% higher in J-J' profile, ∼5% lesser in the K-K' profile, ∼30% higher in L-L profile, and ∼30% higher in M-M' profile than that of the splay fault model. Similarly, the slip rate of the MFT is estimated as: ∼52% higher in I-I' profile, equivalent in J-J' profile, ∼34% higher in K-K' profile, ∼42% lesser in L-L' profile, and ∼10% lesser in M-M' profile than that of the splay fault model.

The model fitting in the single fault model along all the profiles (N-N' to O-O') of the northeast Himalaya is consistent with that of the splay fault model. The slip rate estimates of the MFT and the MHT in the single fault model in both transects are consistent to the slip rate estimates obtained from the splay fault model.

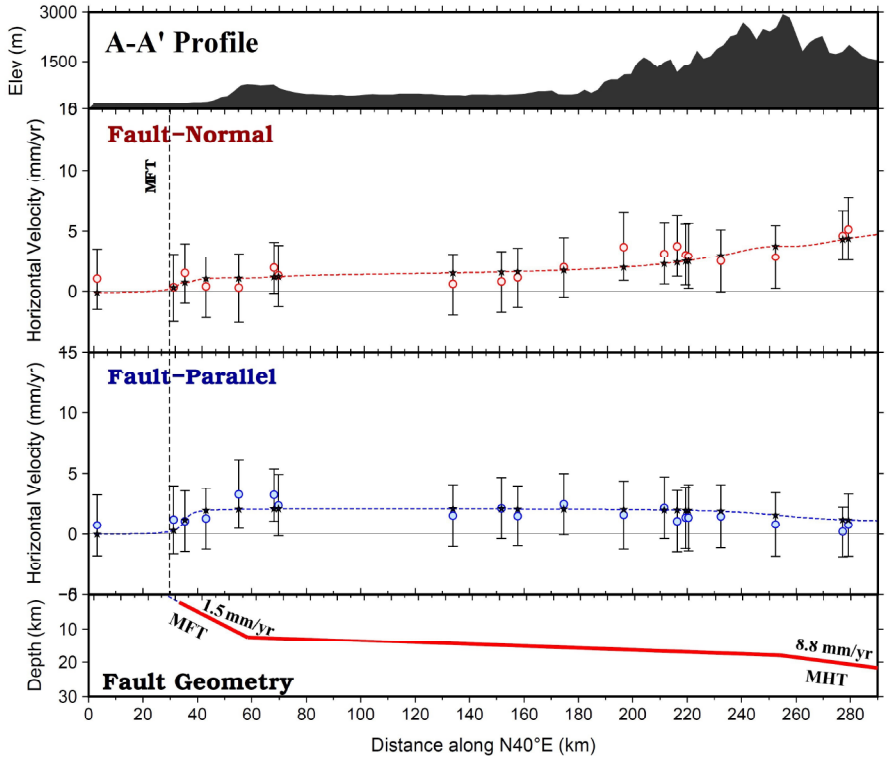

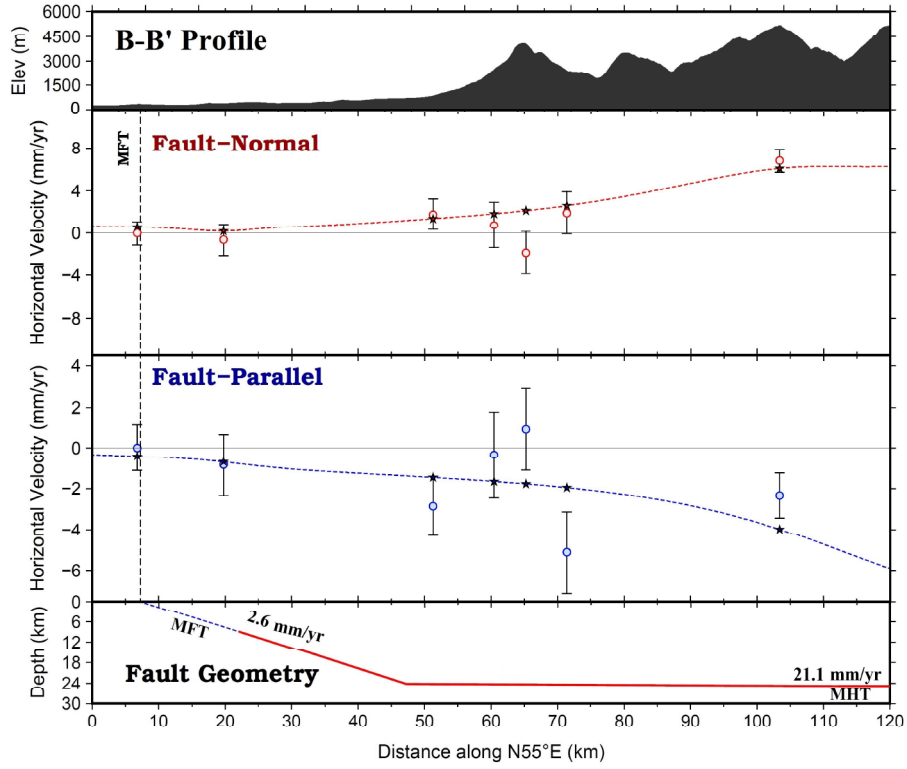
B-B' Profile
Elev (m)
Fault-Normal
MFT
Horizontal Velocity (mm/yr)
Fault-Parallel
Horizontal Velocity (mm/yr)
Depth (km)
MFT
2.6 mm/yr
Fault Geometry
21.1 mm/yr
MHT
Distance along N55°E (km)

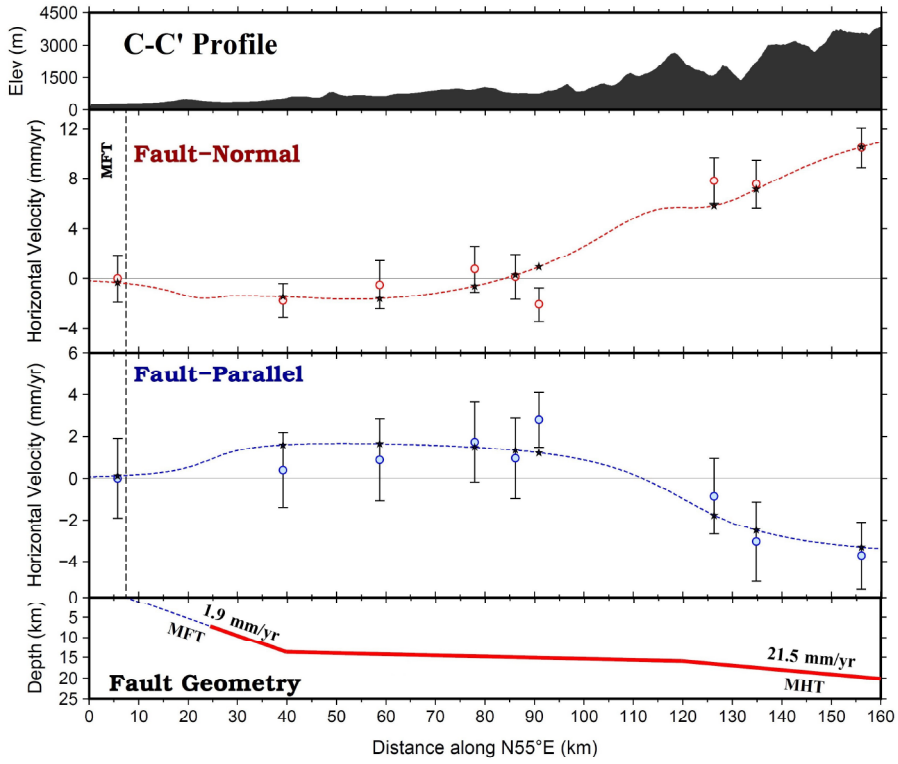
C-C' Profile
Elev (m)
Fault-Normal
MFT
Horizontal Velocity (mm/yr)
Fault-Parallel
Horizontal Velocity (mm/yr)
Depth (km)
MFT
1.9 mm/yr
Fault Geometry
21.5 mm/yr
MHT
Distance along N55°E (km)

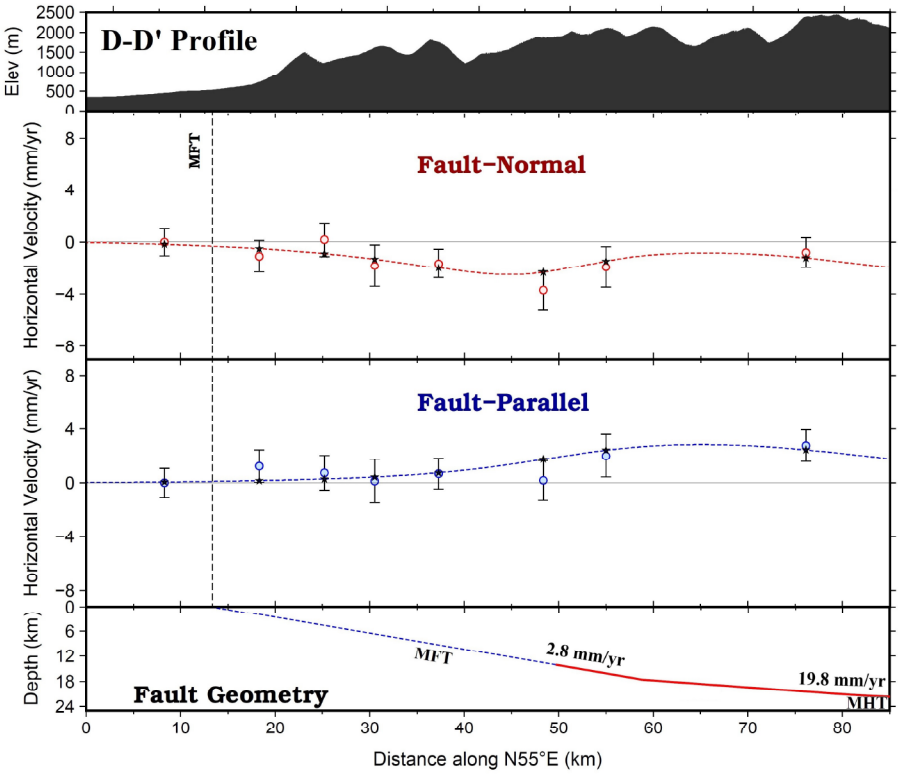
D-D' Profile
Elev (m)
2500
2000
1500
1000
500
0
MFT
Fault−Normal
Horizontal Velocity (mm/yr)
Fault−Parallel
Depth (km)
MFT
2.8 mm/yr
19.8 mm/yr
MHT
Fault Geometry
0
10
20
30
40
50
60
70
80
Distance along N55°E (km)

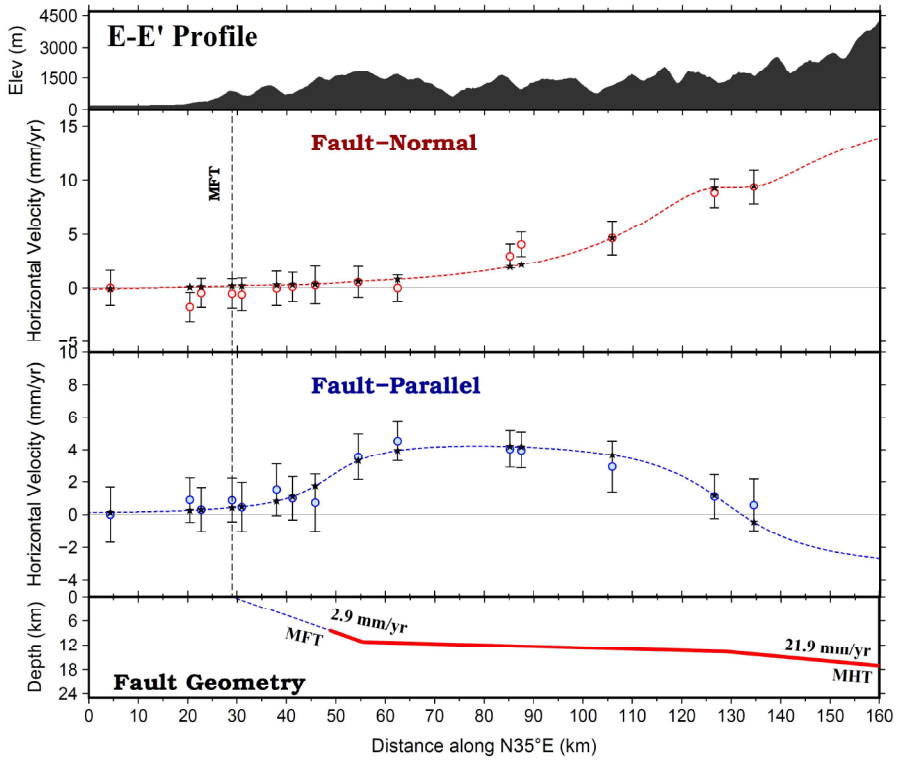
E-E' Profile
Elev (m)
4500
3000
1500
0
MFT
Fault−Normal
Horizontal Velocity (mm/yr)
Fault−Parallel
Depth (km)
MFT
2.9 mm/yr
21.9 mm/yr
MHT
Fault Geometry
0
10
20
30
40
50
60
70
80
90
100
110
120
130
140
150
160
Distance along N35°E (km)

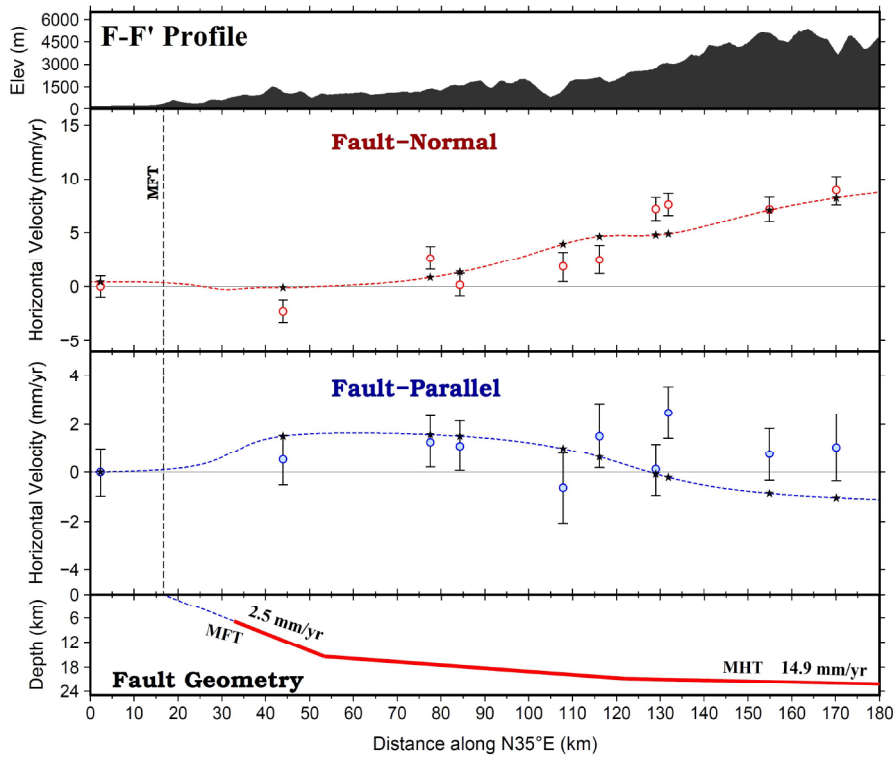
F-F' Profile
Elev (m)
Fault-Normal
Fault-Parallel
Horizontal Velocity (mm/yr)
MFT
Depth (km)
2.5 mm/yr
MFT
Fault Geometry
MHT 14.9 mm/yr
Distance along N35°E (km)

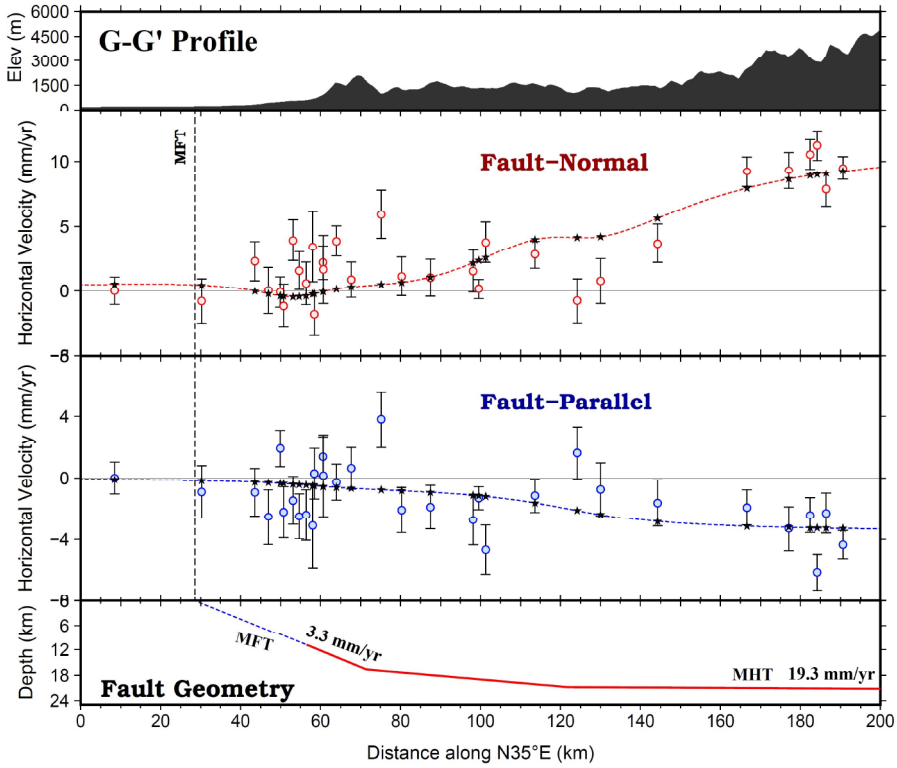
G-G' Profile
Elev (m)
Fault-Normal
Fault-Parallel
Horizontal Velocity (mm/yr)
MFT
Depth (km)
MFT
3.3 mm/yr
Fault Geometry
MHT 19.3 mm/yr
Distance along N35°E (km)

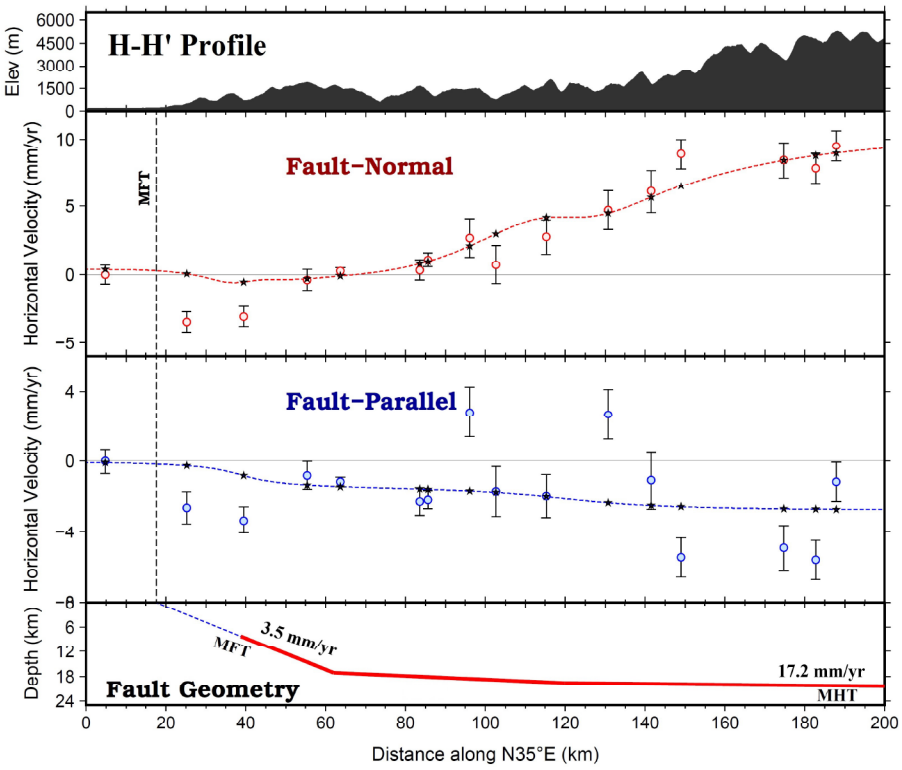
H-H' Profile
Elev (m)
6000
4500
3000
1500
0
Fault−Normal
MFT
Horizontal Velocity (mm/yr)
10
5
0
−5
Fault−Parallel
Horizontal Velocity (mm/yr)
4
0
−4
−8
Depth (km)
6
12
18
24
3.5 mm/yr
MFT
17.2 mm/yr
MHT
Fault Geometry
0
20
40
60
80
100
120
140
160
180
200
Distance along N35°E (km)

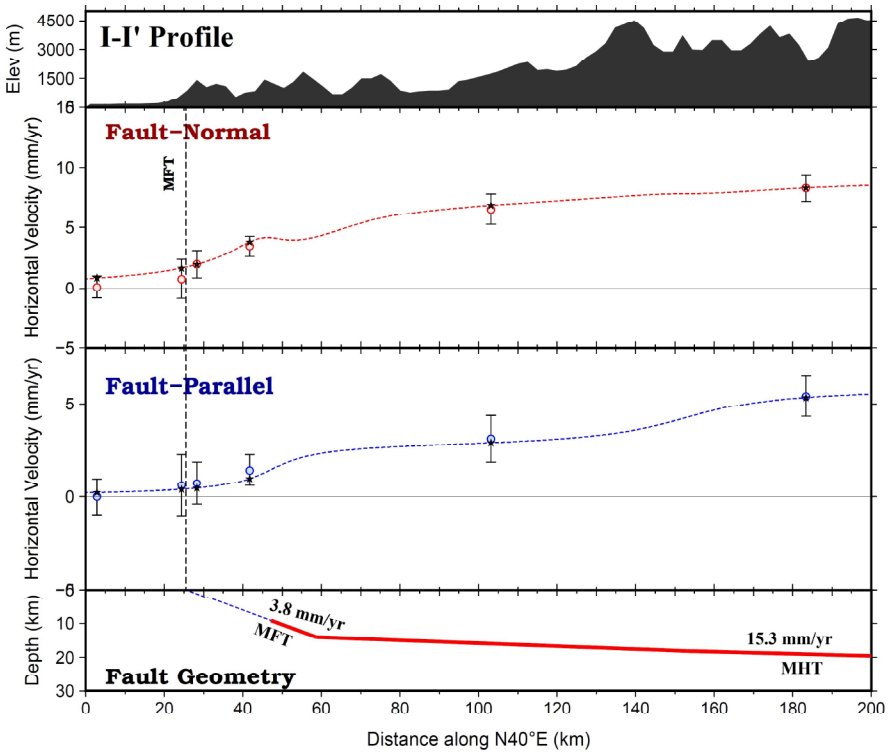
I-I' Profile
Elev (m)
4500
3000
1500
Fault−Normal
MFT
Horizontal Velocity (mm/yr)
10
5
0
−5
Fault−Parallel
Horizontal Velocity (mm/yr)
5
0
−8
Depth (km)
10
20
30
3.8 mm/yr
MFT
15.3 mm/yr
MHT
Fault Geometry
0
20
40
60
80
100
120
140
160
180
200
Distance along N40°E (km)

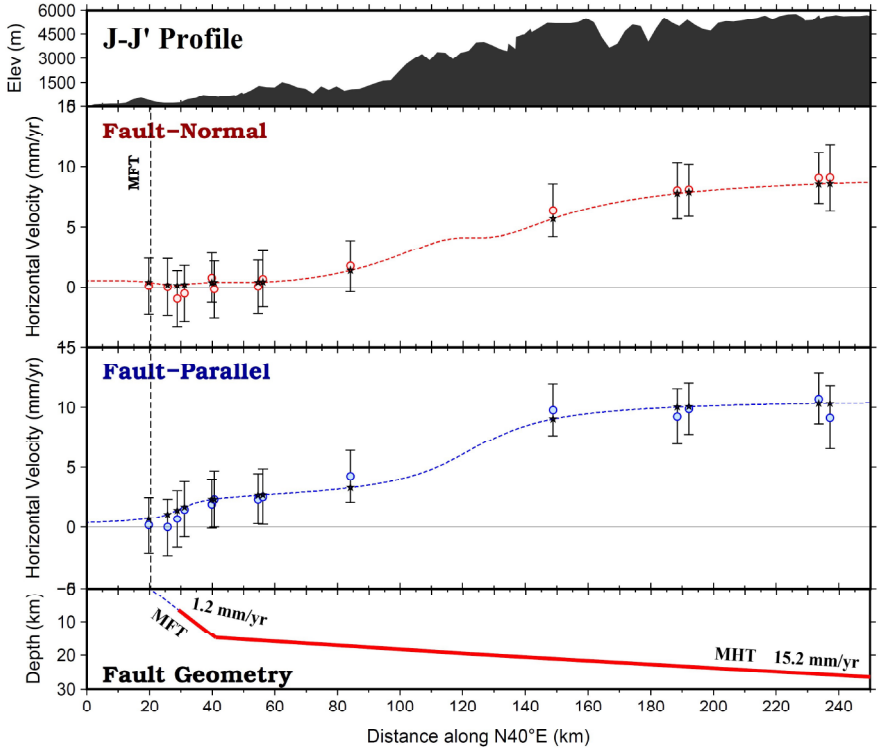
J-J' Profile
Elev (m)
Fault-Normal
Horizontal Velocity (mm/yr)
MFT
Fault-Parallel
Horizontal Velocity (mm/yr)
Depth (km)
1.2 mm/yr
MFT
MHT
15.2 mm/yr
Fault Geometry
Distance along N40°E (km)

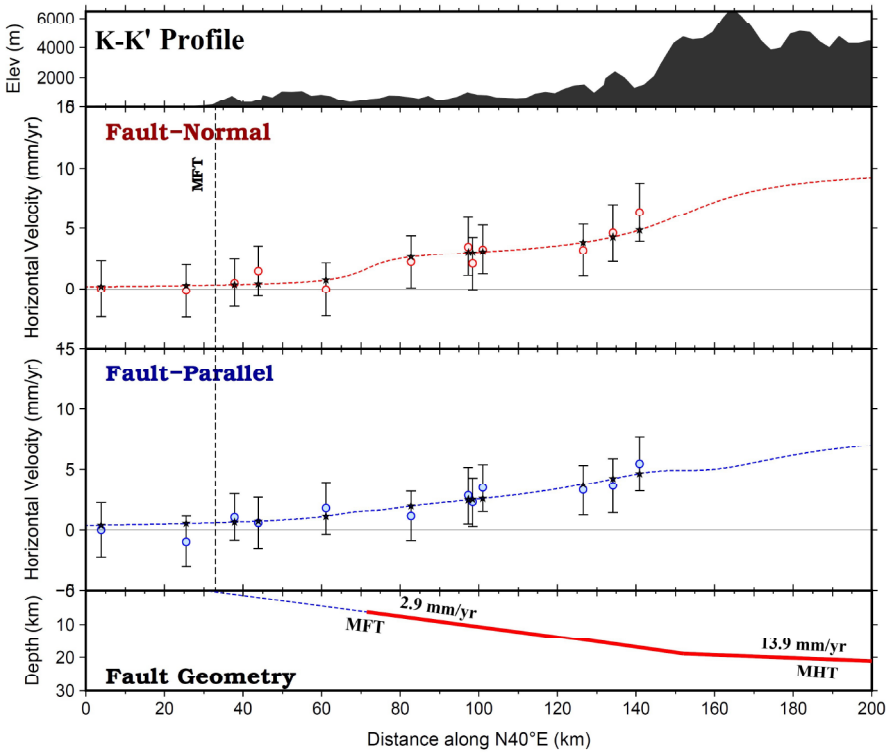
K-K' Profile
Elev (m)
Fault-Normal
Horizontal Velocity (mm/yr)
MFT
Fault-Parallel
Horizontal Velocity (mm/yr)
Depth (km)
2.9 mm/yr
MFT
13.9 mm/yr
MHT
Fault Geometry
Distance along N40°E (km)

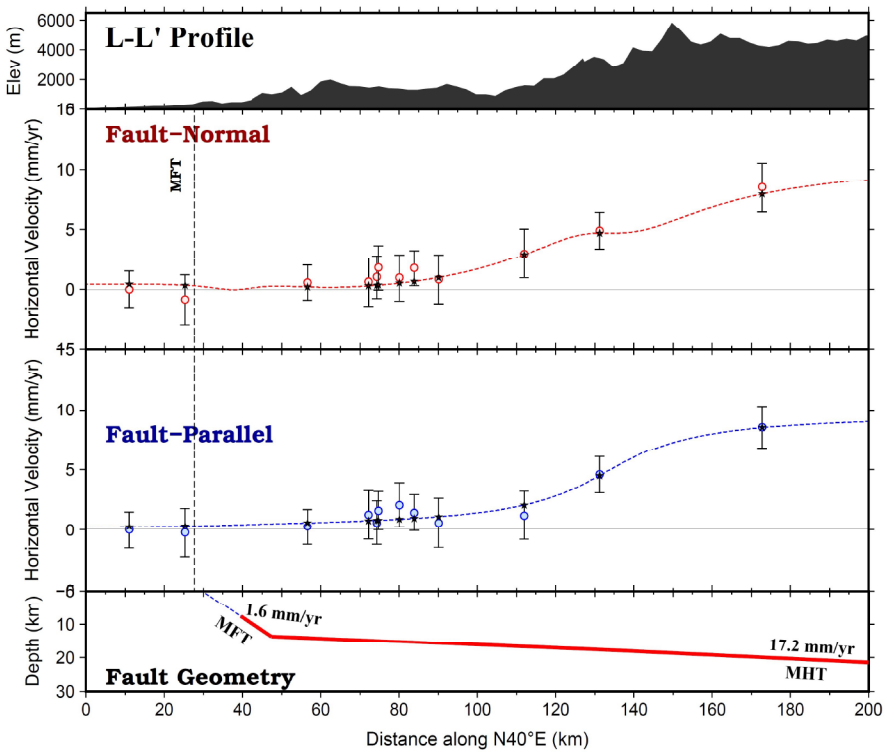
L-L' Profile
Elev (m)
6000
4000
2000
0
Fault−Normal
MFT
Horizontal Velocity (mm/yr)
Fault−Parallel
Depth (km)
1.6 mm/yr
MFT
17.2 mm/yr
MHT
Fault Geometry
Distance along N40°E (km)

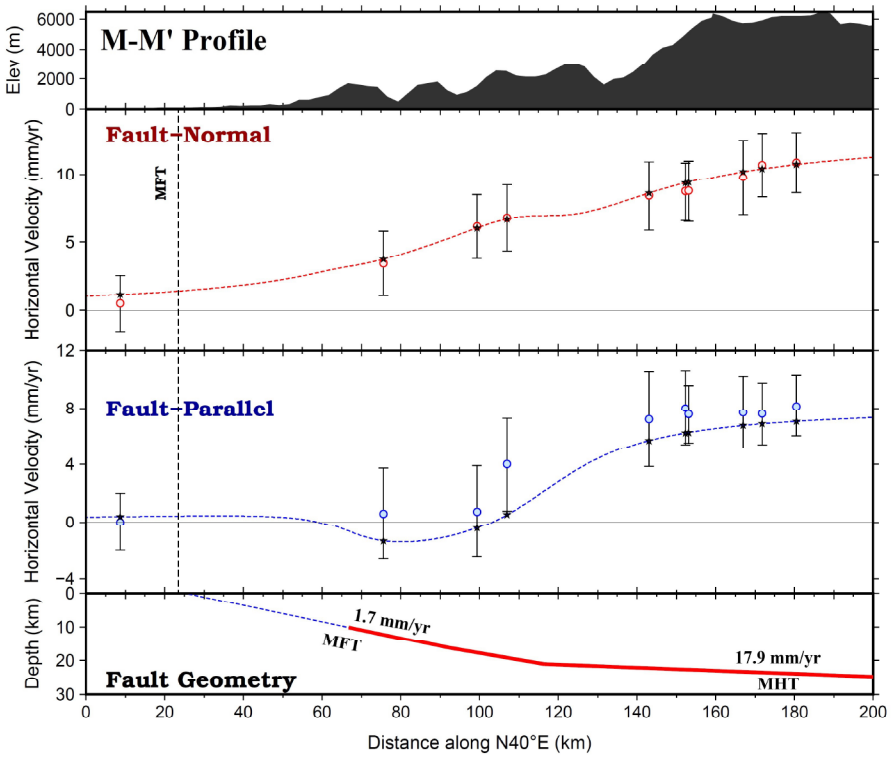
M-M' Profile
Elev (m)
6000
4000
2000
0
Fault−Normal
MFT
Horizontal Velocity (mm/yr)
Fault−Parallel
Depth (km)
1.7 mm/yr
MFT
17.9 mm/yr
MHT
Fault Geometry
Distance along N40°E (km)

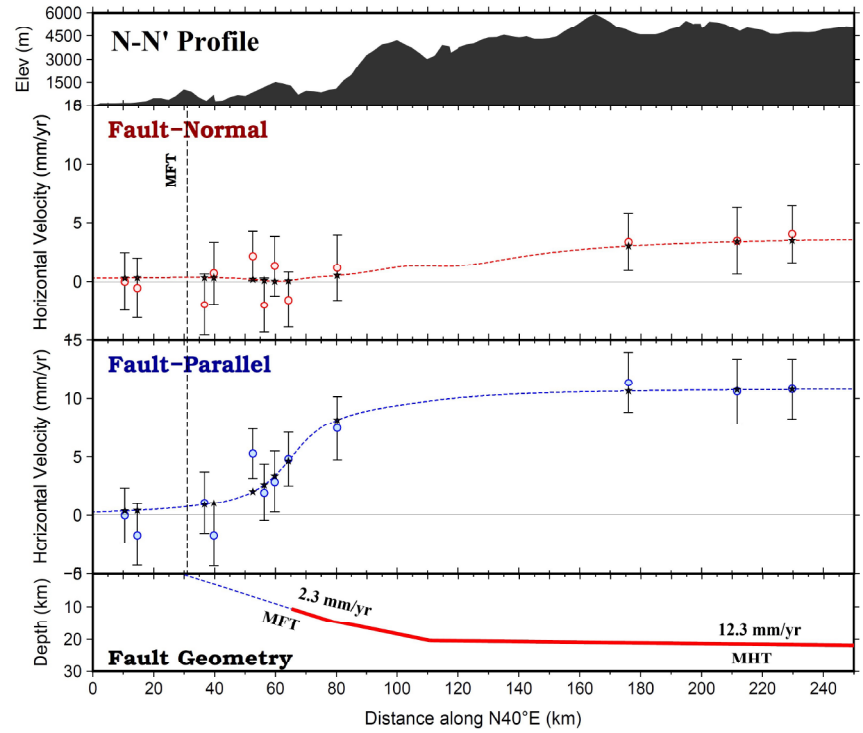

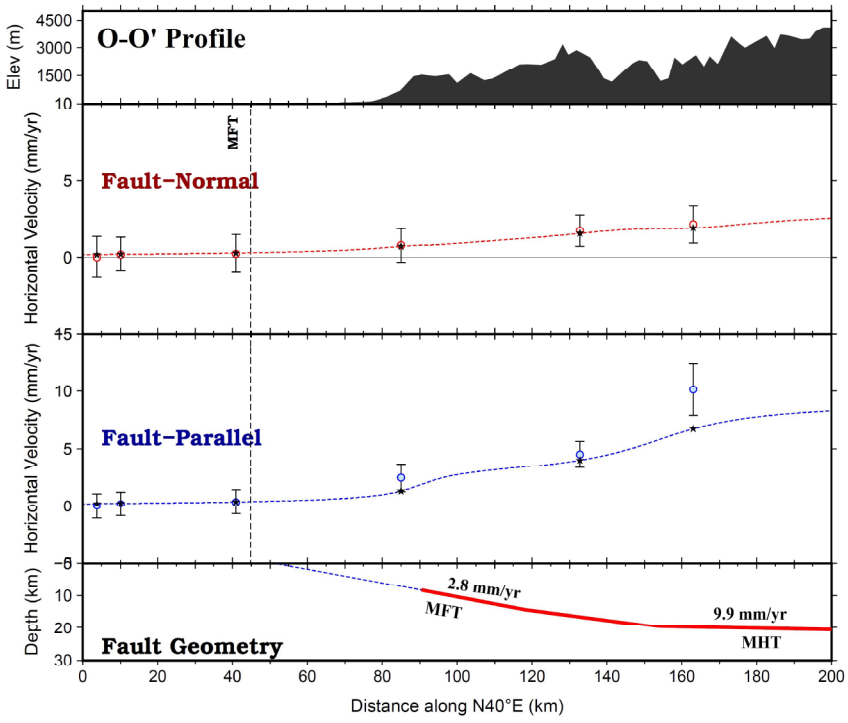

Fig. 4.11: Modeling results across all 15 profiles along the Himalayan arc using a single fault model.

Overall, the model fitting is consistent in all 15 transects along the Himalayan arc. The slip rate estimates of the MFT are higher at an order of two along the northwest and central Himalaya, whereas it is consistent along the northeast Himalaya for both models. Similarly, the slip rate estimates of the MHT are observed to be higher along the northwest Himalaya and consistent along the central Himalaya. The whole comparison implies that the contribution from the slip rates of the splay faults in the total slip rate of the décollement along the northwest Himalaya is significant, though, along the central and northeast Himalaya, it is insignificant.

Table 4.5: Modeled slip rate of MFT and MHT based on a single splay fault model

Area	Profile	Slip rate of MFT (mm/yr)	Slip rate of MHT (mm/yr)
Northwest Himalaya	A-A'	1.5±1.2	8.8±1.2
	B-B'	2.6±0.2	21.1±0.2
	C-C'	1.9±0.9	21.5±0.9
	D-D'	2.8±1.5	19.8±1.5
	E-E'	2.9±1.1	21.9±1.1
	F-F'	2.5±0.7	14.9±0.7
	G-G'	3.3±0.9	19.3±0.9
	H-H'	3.5±1.2	17.2±1.2
Central Himalaya	I-I'	3.8±1.4	15.3±1.4
	J-J'	1.2±2.1	15.2±2.1
	K-K'	2.9±1.1	13.9±1.1
	L-L'	1.6±1.2	17.2±1.2
	M-M'	1.7±1.7	17.9±1.7
Northeast Himalaya	N-N'	2.3±1.4	12.3±1.4
	O-O'	2.8±2.1	9.9±2.1

4.5.3 Implication of seismic hazard along the Himalayan arc

In the previous sections of this chapter, the slip rate distribution along the Himalayan megathrust system has been addressed. Now, in order to examine the earthquake potential along the Himalayan arc, the moment rates are derived from the slip deficit rate of the MFT along different sections of the northwest, central, and the northeast Himalaya. The slip deficit rate for a fault is obtained by subtracting the long-term geological slip rate from the corresponding geodetic slip rate. As the long-term slip rate in the Himalayan arc is available for the MFT only, the earthquake hazard potential is estimated based on the slip deficit rate of the MFT alone.

The rate of geodetic moment accumulation on the MFT is estimated by the equation

$$\dot{M}_0 = \mu \dot{D} A \tag{4.4}$$

Here, μ is the shear modulus that is assumed to be 3×10^{10} N/m^2; $\dot{D}$ is the slip deficit rate; and A is the considered area.

By multiplying the length and depth of the MFT to its corresponding slip deficit rate, the moment build-up rates for different segments are calculated (Table 4.6). It may be noted that to render negligible effects due to rugged surface trace of the MFT, a smooth approximation to the MFT (see Fig. 4.12) is constructed based on the methodology followed by Lindsey et al. (2018) [154]. The length of MFT in each segment is roughly equivalent to the geographic extent in each section. For example, the length of the MFT in the Himachal Himalaya is equivalent to its geographic extent. On the other hand, the depth of MFT in each segment is considered by averaging the modeled depth in each transect of the corresponding segment (Table 4.2 to Table 4.4).

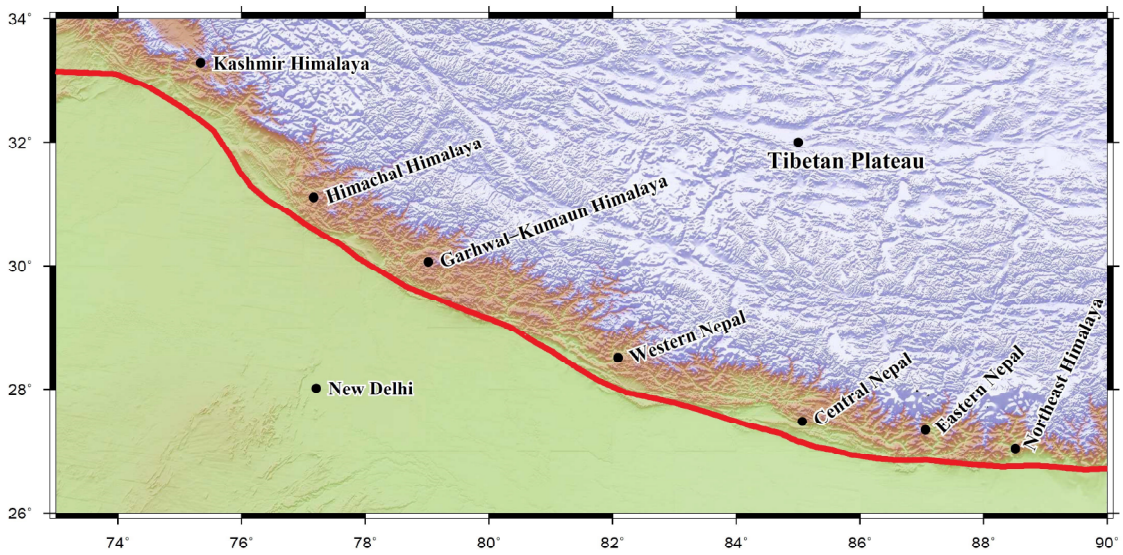

Fig. 4.12: Smooth approximation to the MFT along the Himalayan arc. The red line indicates smooth approximation to the MFT.

The accumulated moment rate varies from 0.4×10^{18} Nm/yr to 2.9×10^{18} Nm/yr (Table 4.6) along the Himalayan arc. Considering a seismic cycle of about 500−1,000 years for a great Himalayan earthquake [219, 277], the earthquake potential is derived for each segment of the arc.

Table 4.6: Earthquake potential in different segments of Himalayan arc

Segment	Long-term slip rate (mm/yr)	Slip deficit rate (mm/yr)	Geodetic Moment (10^{18} Nm/yr)	Magnitude (M_w)
Kashmir Himalaya (Profile A-A')	9.0	7.2	1.1	7.9±0.1
Himachal Himalaya (Profile B-B' to D-D')	10.1	9.6	1.2	7.9±0.1
Garhwal-Kumaun Himalaya (Profile E-E' to H-H')	12.4	11.9	1.7	8.0±0.1
Western Nepal (Profile I-I')	19	17.2	1.9	8.1±0.1

Central Nepal (Profile J-J' to K-K')	21	19.5	2.2	8.1±0.1
Eastern Nepal (Profile L-L' to M-M')	5	2.7	0.4	7.6±0.1
Northeast Himalaya (Profile N-N' to O-O')	21.9	19.2	2.9	8.1±0.1

The earthquake potential along the eastern Nepal turns out to be $M_w \geq 7.6$, the smallest among all segments. This is probably due to the occurrence of the recent large 2015 Gorkha earthquake and the great 1934 Nepal-Bihar earthquake, that have significantly released the accumulated energy [272]. It is observed that there is a potential of a great earthquake in each of the Garhwal-Kumuan Himalaya, western Nepal, central Nepal (which corresponds to the central seismic gap), and the northeast Himalaya. Similarly, there is a potential of a large event ($M_w \geq 7.9$) in each of the Kashmir and the Himachal Himalaya. Overall, the estimation of the earthquake potential of magnitude 7.6−8.1 in the present study agrees to the earthquake magnitude range provided by Bilham (2019) [30]. However, the present estimate is yet smaller than a millenary earthquake of magnitude 9.0 suggested by Stevens and Avouac (2015) [277].

4.6 Summary

Using the updated interseismic GPS velocity field, a Bayesian inversion dislocation splay fault model is used to describe and interpret the fault geometry and slip partitioning of the thrust fault system along the Himalayan arc. The present analyses lead to the following results:

1. The persistent locking behavior of both MFT and MBT is observed along the entire Himalayan region, whereas the estimated slip rate of MCT (∼4.2 mm/yr to ∼13.8 mm/yr) suggests that it is currently active.

2. The MHT has an estimated average slip rate of $\sim 13.8 \pm 3.1$ mm/yr along the Himalayan arc.

3. The single-fault model provides a higher estimate of slip rates for the MFT and the MHT along the northwest Himalaya. However, the results (slip rates) are comparable to the splay-fault model along the central and the northeast Himalaya.

4. The earthquake potential is found to be higher ($M_w \geq 8.0$) along the central seismic gap (Garhwal-Kumaun Himalaya, western and central Nepal) and the northeast Himalaya, whereas it is smaller ($M_w \geq 7.6$) along the eastern Nepal.

As a whole, the 2D splay-fault Bayesian inversion modeling in this study provides a high-resolution image of the present-day fault kinematics along the Himalaya and thus contributes significantly to the improvement of the time-dependent seismic hazard analysis.

The present chapter has discussed fault kinematics of the megathrust system and its implication to the seismic hazard along the Himalayan arc. The next chapter, Chapter 5, will discuss the spatial distribution of earthquake potential along the Himalayan arc.